UNIVERSITY OF CONCEPCIÓN
SCHOOL OF ENGINEERING

MULTIPHYSICS ANALYSIS OF A HIGH LOSS INDUCTION MOTOR

By Matias Sebastián Jiménez Molina

Thesis presented to the School of Engineering of University of Concepcion to qualify for the master's degree

Supervisor:

Juan Antonio Tapia Ladino

Werner Jara Montecinos

Committee:

Aníbal Valenzuela Latorre

Carlos Medina Muñoz

October 2020

Concepción, Chile

Abstract

In Carelian Drives and Motor Centre (CDMC) different models to predict an electric machine behavior are been developed. Among them, a thermal model is needed to simulate the temperature distribution inside a motor. Since is difficult to identify the losses in machines with high efficiency, a test motor built with a high loss electrical steel is considered to build a simple and accurate model, which is the goal of this thesis.

This work presents an electromagnetic and thermal analysis of an induction motor manufactured with an electrical steel which presents high iron losses to identify the eddy current and hysteresis losses more easily which are one of the main sources of heat in an electric machine.

First, the electromagnetic analysis is carried out to find the losses distribution inside the machine. In order to do this, an analytical approach was used to find the Joule stator and rotor losses. The iron losses were found using an FEA software, where using the mass-loss curve provided by the manufacturer, the coefficients needed for the calculation were obtained. These values are going to be use as input data for the thermal analysis.

Then, the thermal analysis was done, first with the lumped parameter method (LPM). With this technique, a thermal circuit was built to obtain the temperature distribution inside the induction machine. Using the conductance matrix method, as in electric circuits, the node's voltages were obtained, which in the context of thermal networks, are the temperature of each part of the motor.

Also, a finite element method analysis (FEA) was carried out to solve the heat transfer problem inside the motor and obtain the temperature distribution. After the simulation were done, the LPM results and the FEA results were compare to experimental data to validate the models. The results showed a better accuracy from the FEA model, but the LPM model only reach around a 5% error with respect to the validation data.

In conclusion, both models have satisfactory results taking into consideration that the LPM model require much less time to setup and less computation power to be solved. The FEA model is more accurate but require more expertise from the user, and adequate hardware to be implemented, but it can be applied to any geometry so is more versatile.

Acknowledgments

Thanks to all my family and friends who support me and help me when I need it.

Thanks to my supervisor, Professor Juan Tapia, and all the member of the faculty and the department for guide me and help me through the past two years.

Thanks to Professor Pia Lindh and all the Lappeenranta University of Technology team, who help me during my internship earlier this year and during the realization of this project.

Finally, thanks to all the people who, in some way, help me during the past years.

Contents

List of Figures

List of Tables

List of symbols

F : Force on the conductor

i : Current

l : Length

B : magnetic flux density

T : Torque

r : radius

e_{ind} : induced voltage

n_s : synchronous speed

f : frequency

p : number of poles

s : slip

n_m : mechanical speed

R_{cond} : resistance of the conductor

I_{cond} : current circulating on the conductor

l_{cond} : length of the conductor

A_{cond} : cross-section area of the conductor

R_f: Final resistance

R_i: initial resistance

α: temperature coefficient of a material

μ: dynamic viscosity of the fluid

C_p: specific heat

k : thermal conductivity

ρ: density

V: upstream velocity

l_c: characteristic length of the geometry

μ_k : kinetic viscosity of the fluid

g : gravity acceleration

β : coefficient of volume expansion

v: rotational speed

δ: air-gap length

Abbreviations

CAE: Computer aided engineering.

CAD: computer aided design.

LPM: Lumped parameter method.

FEA: Finite element analysis.

CFD: Computational fluid dynamics.

Chapter 1.   Introduction

1.1   Preface

Approximately 70% of the energy generated for industrial consumption and 50% of the world's capacity is used to power electric motors [1], [2]. The importance of the improvement in electric machines efficiency relies in the fact that more than 10 percent of the energy consumption can be saved in some developed countries [3]. Since the first prototypes in the early 19th century, electrical machines have not only modified their topology. Materials, applications, and even design and manufacturing processes have changed dramatically over the years.

As new applications gain ground due to technological advances and lower costs, it is essential that the area of electrical machines must adapt to these changes. New designs that allow achieving greater efficiency and power density are one of the main objectives when creating a new prototype for applications that are increasingly popular such as electromobility, wind generation, etc.

Depending the type of electric machine, the total energy loss during the operation vary between 5%-25% [4], which translate in heat generation inside the motor. The rise of the temperature can impact the overall performance of the equipment and even reduce its lifetime. There are several factors that can cause a failure in an electric equipment. Among them, the temperature is one of the elements that limit the power output according to the rated values given by the manufacturers. High heat production in a motor can cause problems such as early aging of the winding insulation, deterioration of bearing lubricants and mechanical stress which translates in premature failure. Because of this, a thermal analysis during the design process is fundamental to avoid failure and maximize the reliability of the machine.

The design workflow is another point where an optimization can be done. Reducing the computation time and the hardware requirements for the simulation and analysis could be crucial to the development of scientific project centered in electric machine design with academic purposes. In teams with a limited number of people, increasing the efficiency of the design process and reducing the time consumption for each task is important. The use of only one method (Finite element analysis for instance) could facilitate the coupling between the electromagnetic, thermal and structural design.

Also, for one user that already have experience in electromagnetic analysis with FEA, would be easier to develop a thermal model in this case, saving time.

The motivation of this work relays in find alternative procedures to execute thermal analysis to solve the heat transfer problem inside an electric machine. The process of obtaining experimental data about the losses and temperature distribution inside an electric motor is a complex task due to space and hardware limitations. This work approach this problem, modeling a high loss induction motor to ease the losses measurements and predict the temperature values in zones that usually are not accessible with sensors, such as airgap, stator slot winding and in rotor iron and aluminum cage.

For an unexperienced user, it would be useful to find other methods to develop a multiphysics model of a motor that require less time to learn and apply. The industry standard is to use CFD in the fluid flow calculation. This is an expensive software and the hardware require to properly solve the simulation scenarios range from US 5.000-45.000 or even more depending the nature of the problem to solve.

At present there is not many publications about the usage of FEA instead of CFD in thermal analysis. Also, an alternative procedure for faster and accurate thermal model in electric machine design has not been explore as much, then this work covers that ground offering some guide in that regard.
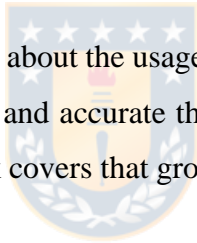
1.2 Hypothesis

It is possible to simplify the process of thermal analysis in the design of an electrical machine with respect to the industry standard - which is CFD - using alternative analytical and numerical methods that allow to decrease the use of computational resources and facilitate the integration of Multiphysics models, without compromising the precision of the results.

1.3 Objectives

1.3.1 General objective

➢ Build a numerical and analytical based model to obtain the temperature distribution inside the induction motor and validate the results with available experimental data.

1.3.2 Specific objectives

➢ Use analytical and numerical method to obtain the loss distribution inside the induction machine and use it as inputs for the thermal models.
➢ Identify and characterize the heat transfer process inside the induction motor and determine the interaction between each of the parts.
➢ Use the lumped parameter method to build a thermal circuit representing the geometry to obtain the temperature distribution calculating the node voltages.
➢ Built a finite element analysis model with the aid of a CAE software, to simulate the heat transfer phenomena.
➢ Validate the results of the two models with experimental data, compare them and conclude about the advantages and disadvantages of each one.

1.4 Scope of the thesis

This work was done with experimental data provided by the Lappeenranta University of Technology (LUT) machine design team obtained from a test motor located in Carelian Drives and Motor Centre

(CDMC). The simulations are made in a multiphysics finite element commercial software (Ansys v18.1) for the electromagnetic and thermal analysis.

1.5 Topics and methodology

In chapter 1 a brief introduction to the work is done and the hypothesis objectives and scope of this work is presented. In chapter 2, a bibliography review was done including the most important topics related to this research. Chapter 3 is about the electromagnetic analysis of the induction motor, where the losses distribution inside the IM was obtained in order to use as input values in later studies. Chapter 4 presents the thermal analysis for the induction machine, which is one of the main goals of this thesis. This is done with two methods, the lumped parameter method and by finite element analysis, validating the results with experimental data provided by the LUT team. Finally, the conclusions about the work are established and some future work regarding the study is commented.

Chapter 2.   Bibliography review

In this section, the most important concepts related with this thesis research are reviewed. These concepts, due to this topic nature, comes from different specialization engineering areas, therefore for the reader that isn't too familiarized with some of these ideas, it will be helpful to the better understanding of the process of the study and the conclusion regarding the results. In the following sections, the phenomena related to the electromagnetism, heat transfer, material science, numerical methods and multiphysics analysis and design workflow are revised, always taking in account the applications regarding the electric machines.

2.1 Material selection

The materials behavior is a very important aspect to considerate when analyzing an electric machine performance because of the large impact that the different options and combination of cost/quality can have on the motor results.

The main active parts participating in the electromagnetic and heat transfer process in an electric machine are the stator and rotor core, windings, insulation materials, the shaft and the housing, so it is convenient to analyze the typical manufacturing material present in this elements and to include some studies regarding new configurations and materials presented in some newer research.

2.1.1 Magnetic materials

Magnetism is a phenomenon that is present everywhere, either in the inside of an electric machine, or the magnetic shield surrounding the Earth that protect us from the outer space radiation. This is how all the materials are affected by this energy to a greater or lesser degree to which according to their reaction we can classify them as diamagnetic, paramagnetic or ferromagnetic materials.

Diamagnetic materials are those which are not perturbated by external magnetic fields and maintain a neutral magnetic moment in the presence of these (copper, silver, water, etc.). the paramagnetism is a property that indicates a net magnetic moment grater that zero in some materials making them to react to the external field in some degree depending the paramagnetic level of the material (air, aluminum, etc.). Ferromagnetic materials are those in which the magnetic moments associated with its molecules

easily respond to an external field, so they are easy to magnetize (iron, cobalt, nickel, etc.). Besides from the categories mentioned above, the material can also be classified into other groups which are detailed in [5], [6], however, there is another category related to the application of these in the electric machine context. These are the soft and hard magnetic materials, discussed below.

- *Soft magnetic materials*

These are materials widely used in electromechanical conversion devices and transformers. They are characterized by being very easy to magnetize and demagnetize, due to their high magnetic permeability, which is why they are elements that allow the conduction of magnetic flux efficiently, with lower losses associated with this phenomenon.
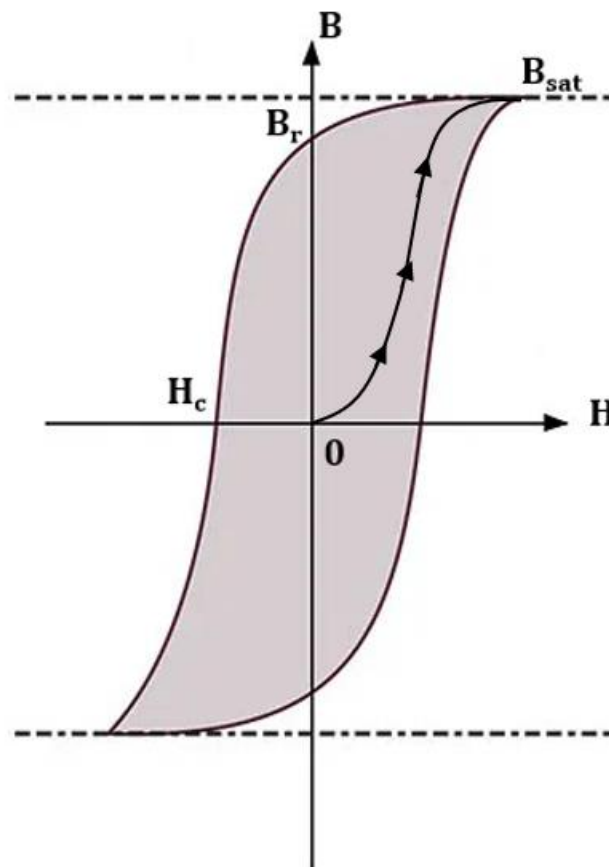
Figure 2.1 Hysteresis curve of a material *(own source)*.

An important aspect when analyzing the magnetic properties of a material is to observe its hysteresis curve. This curve shows how the material responds to magnetization and demagnetization processes

due to the presence of an external AC magnetic field. Figure 2.1 shows a typical cycle where the values of greatest interest are $\mathbf{B_{sat}}$, the saturation point, where almost all of the component's magnetic domains are aligned and a variation in the intensity of the magnetic field generates very small flux changes within of the material. $\mathbf{B_r}$ is the residual magnetic flux density, which is the magnetic flux that remains in the material when the external magnetic field is reduced to zero. $\mathbf{H_c}$ indicates coercivity, which is the amount of magnetic field that needs to be applied in the opposite direction to misalign the magnetic moments of the material and eliminate the remaining flux in it. Finally, the area enclosed by the hysteresis cycle represents the energy used [7].

A soft magnetic material is characterized in its hysteresis cycle by a low remanence and coercivity which is ideal for operation in transformers and electrical machines because of flux variations will generate lower iron losses compared to other types of materials. Iron and different alloys meet the characteristics mentioned above, making them ideal for use in motors and generators, which are discussed below.

Carbon steel was the first material used in transformers and electrical machines, but due to the low efficiency achieved by motors built from this material, today it is only used in the manufacture of small motors where efficiency is not as important compared to the lower cost [5].

In the early 1920s [6], the addition of small amounts of silicon to iron is found to increase the strength of the material and decrease its coercivity. These new properties allow this new alloy, called electric steel, to become the new standard in commercial motors due to the great reduction in hysteresis and eddy currents losses. Currently, a silicon concentration between 2-3% is used in most cases. Among the electric steels we have those of non-oriented grain, the most used option currently, which have high resistivity and permeability. It is an isotropic material (similar magnetic properties in all directions) since no special processes are carried out during its manufacture. In addition, there are grain-oriented electric steels, which is anisotropic and can withstand a greater amount of magnetic flux in the rolling direction, making it especially useful in the construction of transformers, although it results from applying additional processes to the iron, which increases its cost [8].

New studies in recent years have emerged to improve the efficiency of electric machines in relation to new alloys or optimization of production processes for electric steel. A higher concentration of silicon (up to 6%) would greatly improve the magnetic performance of the material, however, the mechanical properties would worsen, as the steel sheets become much more brittle, increasing the

chances of failures, such as cracking which translates in worse magnetic performance [9], [10]. Other alloys such as permalloys, amorphous alloys or nano-crystalline compounds have received a lot of attention from the research community, due to the better performance that they can present in certain specific applications. [5], [6], [11].

- *Hard magnetic materials*

In this category are the permanent magnets (PM), materials that are intended to supply a constant magnetic field in a certain region of space. The characteristic that allows magnets to provide a constant flux is their great remanence and high coercivity. As shown in Figure 2.2a, the hysteresis cycle of a permanent magnet is much larger, making it a material that was not built to undergo magnetization and demagnetization processes. The great remanence allows it to deliver a constant magnetic field and its coercivity value indicates that it is resistant against external excitations as would be the case with the interaction with the stator winding in an electrical machine.
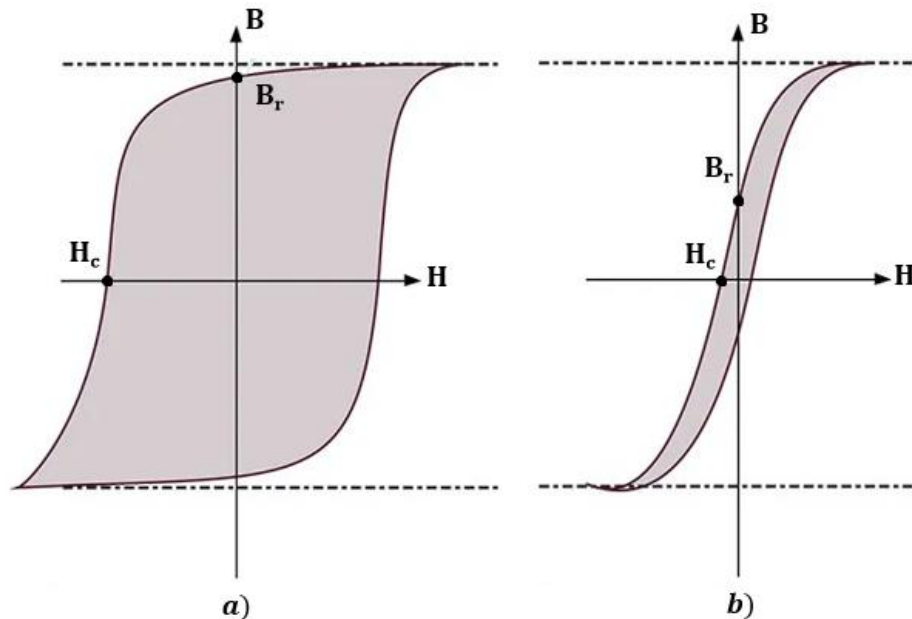
Figure 2.2 Hysteresis curve comparison for a) hard magnetic material and b) soft magnetic material *(own source).*

The effect of external magnetic fields is generally a problem in materials with low coercivity such as ferrite magnets or based on Nickel-Cobalt (AlNiCo). When an external flow is applied, the working

point within the B-H curve of the material is changed. At the time of removing the external excitation, it does not necessarily return to the same point of previous operation, so the magnet would present a small irreversible change, which would alter its magnetic characteristics. Also, in the event of a short circuit in a motor, the large currents produced can generate a magnetic field intensity greater than the coercivity of the PM, which would generate the total demagnetization of this [5].

Temperature is another very important factor in the stability of magnets. There are two types of changes in the operation of the material, reversible and irreversible.

The increase in temperature will cause a decrease in the magnetic flux density that the magnet can provide. However, if the temperature returns to its original value, the operating point will be the same as before, making it a reversible change. Table 2.1 shows characteristic values for magnets of different composition [5], [7].

Table 2.1 Some permanent magnet properties.

Material	Br, T	Hc, kA/m	$(BH)_{max}$, $kJ/m3$	$Tmax$, $°C$	Tc, $°C$	α_B, $\%/°C$	α_H, $\%/°C$
Ferrita	0.38	191.04	27.86	200	~700	-0.20	0.27
Alnico 9	1.12	109.45	83.58	500	~1100	-0.02	-0.01
SmCo	1.07	776.10	206.96	350	~1000	-0.03	-0.20
NdFeB	1.29	987.04	318.40	170	~600	-0.10	-0.40

In table 2.1 the value T_{max} represents the maximum operating temperature recommended by manufacturers where the magnet does not undergo irreversible changes. T_c indicates the Curie temperature, which is where the magnet undergoes total demagnetization.

Finally, even the geometry and magnetization direction play a fundamental role with respect to the performance of IP. In some publications, such as those carried out in [12], [13] give an account of different advantages and disadvantages that the simple fact of choosing the correct shape of the magnet that works best according to the type of machine and desired application can have.

2.1.2 Other materials used in electric motors

Although magnetic materials are of great importance in the construction of an electric machine, other components that make up a motor will be analyzed below.

- *Windings*

The coils inside a machine consists of the copper conductors surrounded by insulation that can be made of organic materials such as paper or cotton with epoxy resins for low temperatures or inorganic materials such as mica, fiberglass with epoxy resins, or silicone for insulation of higher temperatures [14]. These materials are of utmost importance since they do not allow contact between the conductors, preventing short circuits and therefore motor failures. Table 2.2 shows the maximum temperatures allowed for each insulation type according to the international standards.

Table 2.2 Winding insulation types in electric machines.

Insulation type	Maximum temperature according to IEC 60085 [15]
A	105
E	120
B	130
F	155
H	180

Although it seems that there are not many research interest based on this, recent investigations focused on materials science, reveal new types of insulation materials that improve the heat extraction capacity of equipment such as transformers or electrical machines [16], [17]. Also, there are some studies that seek to improve the manufacturing processes of conductors in order to reduce costs due to uses that have been getting more attention in recent years such as electro mobility and renewable energy applications [18].

- *Composite materials*

Composite materials have been around for a long time. Elements such as concrete, adobe bricks, among others have surrounding us for thousands of years. In the second half of the 20th century, more complex materials began to emerge and research around them increased significantly. Over the years, more efficient and modern manufacturing methods allow increasingly sophisticated compounds to be built without the need to raise costs abruptly, making composite materials a viable alternative for various applications, among which recently we can include electric machines.

In addition to the materials that are used in the insulation of the coils, other resins can be used to increase the heat transfer capacity from the stator to the casing and then be removed into the environment [19], [20], or the addition of conductive paths in the axial direction to evacuate the heat in the housing endcaps in an machine [21]. Even replacing iron cores with magnetic composites or using a rotor built from fiberglass has some advantages that in some specific applications are worth considering. [22]–[24].

2.2 Electromagnetic analysis

In the process of designing an electrical machine, the analysis of the magnetic and electric circuit of the equipment is one of the first steps and the results will be input values for subsequent thermal (losses distribution) and structural (Forces and torque calculation) studies.

This study consists of obtaining, either by analytical methods or simulations, the performance of the machine at different points of operation to predict its behavior. Next, fundamental concepts to be considered at this stage of the design will be discussed in order not to leave gaps when showing the development of the work of this thesis.

2.2.1 Force and torque production in an electric machine

The torque produced by an electric machine is given by the interaction of the magnetic fluxes of the stator and rotor. The force acting on the conductor of a motor is given by the Lorentz force shown below (see figure 2.3).

$$\boldsymbol{F} = i(\boldsymbol{l} \times \boldsymbol{B}) \tag{2.1}$$

Like any force, if it is applied to a mass capable of rotating, then at a distance r from its axis a torque given by Eq. (2.2) is produced.

$$\boldsymbol{T} = \boldsymbol{r} \times \boldsymbol{F} \tag{2.2}$$

This principle together with the fact that when particles are place in a large external magnetic field, their spin will align with that field (lower energy situation) allows electrical machines to maintain a rotational or translational movement.
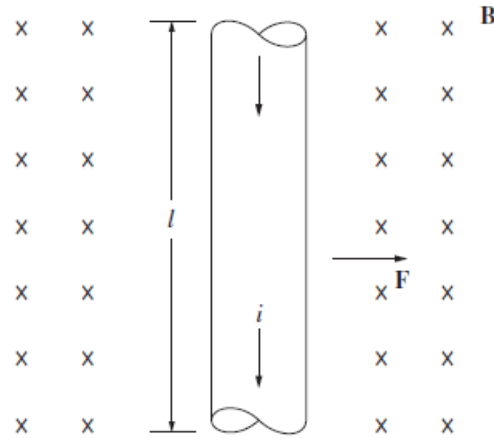
Figure 2.3 Force on a conductor [25]**.**

A constant torque value in a steady state operation is usually a desired aspect of machine behavior. In many applications, precise torque control without variations is required, so analyzing the torque components that may be present in the operation of the motor is of great importance as considerations when proposing new designs.

The term pulsating torque refers to any source of divergence from ideal behavior, either by the nature of the machine or the control method used [25]. The pulsating torque components that can occur in the operation of the equipment are defined below.

This variation occurs mainly due to the interaction of the harmonic components between the magnetomotive force and the magnetic flux density in the air gap. They can also be a product of factors not related to the geometry of the machine, such as the presence of converters and the control methods used in the drive.

In [26]–[30], analysis of the components of the pulsating torque is carried out, analytical expressions are obtained, methods for the reduction of these effects are studied, and even less known techniques are used, such as the use of Kalman filters to identify the unwanted components or techniques associated with the artificial intelligence (fuzzy logic) to optimize control of the converters.

The structural analysis of the electrical machine is also very important within the design process. Although this study requires several input values, in the electromagnetic context, the magnetic pull due to the attractive forces that exist between the rotor and stator is a very important piece of information to consider due to the mechanical stress results that can be indicative of possible failures in some components inside the motor.

While on a machine that has gone through a manufacturing process with no error within it, radial forces should be canceled out for perfectly concentric rotors and stators. However, this situation is not realistic, since the construction of the motors and generators is not free from defects, which generate small eccentricities that, depending on the size of the equipment, may be an important factor to consider [31]–[33]. In addition, modular nature machines, such as some of the large mills in the mining industry must withstand these forces on the bolts that hold each pole in place [34] an therefore, the mechanical stress in these components needs to be calculated in case the power output of the motor must be increased.

2.2.2   Induction machine basics

An induction motor is one of the most used electric machines in the industry nowadays. Figure 2.4 shows a typical induction motor, figure 2.5 and figure 2.6 shows a radial view and the main parts of a squirrel cage induction machine respectively, which is the type of motor studied in this thesis.
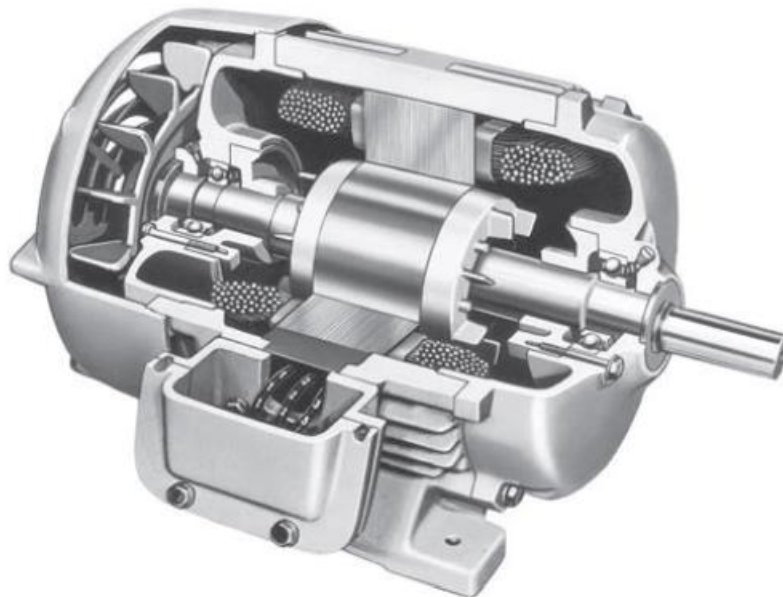
Figure 2.4 Typical induction motor diagram [25]**.**
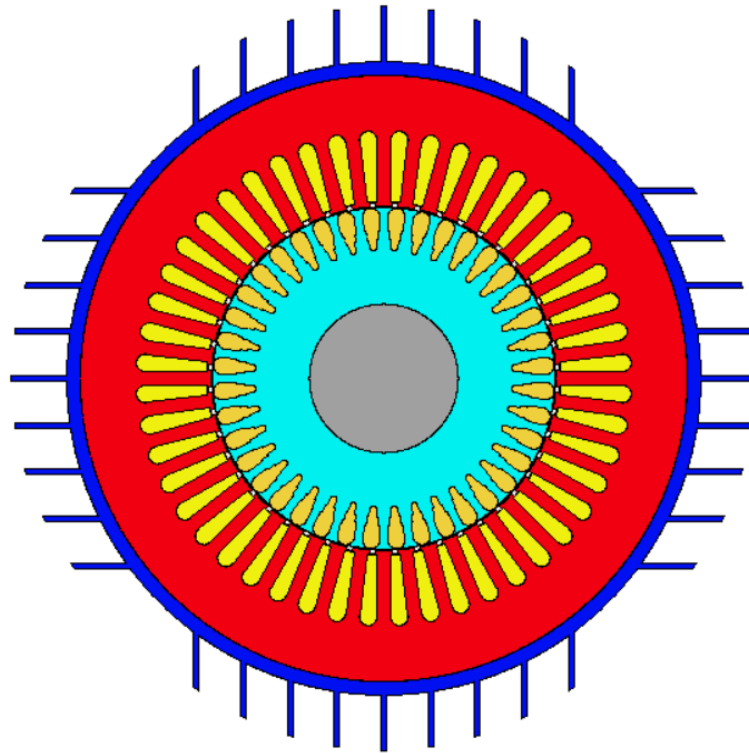
Figure 2.5 Radial view of an induction motor *(own source)*.
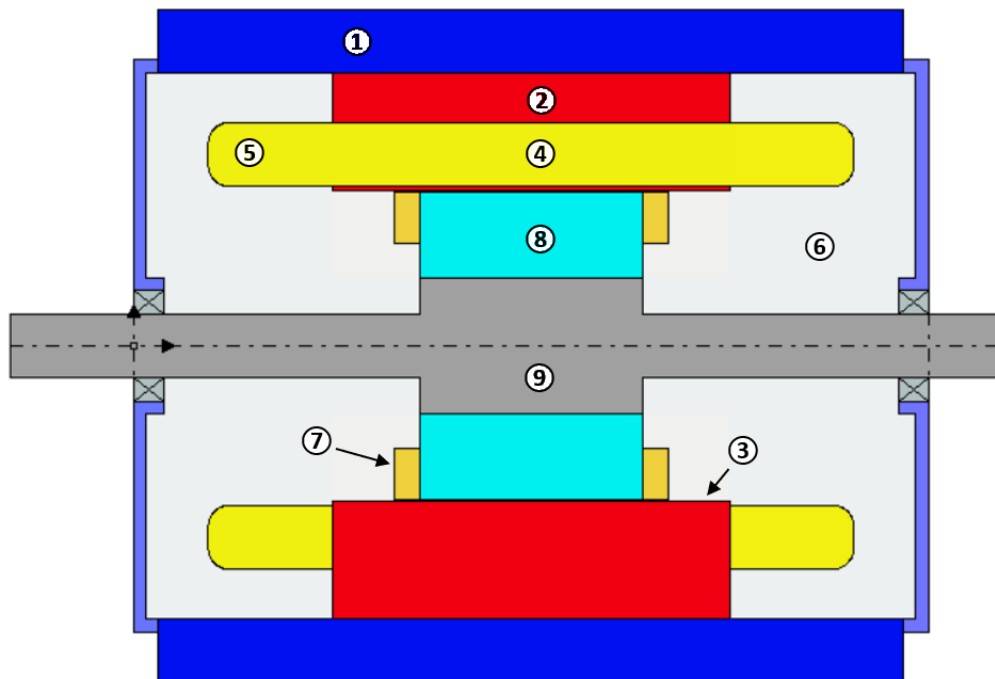
Figure 2.6 Main parts of an induction motor. 1. Frame, 2. Stator iron, 3. Stator tooth, 4. Stator winding. 5. Stator end winding, 6. Motor end space, 7. Rotor winding, 8. Rotor iron, 9. Shaft *(own source)*.

When the machine is supply by three phase voltage, a rotatory magnetic field appear. The variable magnetic field induces a voltage in the rotor cage given by

$$e_{ind} = (v \times B) \cdot l \tag{2.3}$$

This voltage produces a set of currents that creates another rotating magnetic field that follow the one generate by the stator currents. The stator magnetic field rotates at the synchronous speed as follow

$$n_{sync} = \frac{120f}{p} \tag{2.4}$$

Since the machine do not produce torque when the stator and rotor magnetic field rotate at the same speed, the rotor speed is lower than the syncronous speed an the slip of the motor at one operation point is given by

$$s = \frac{n_{sync} - n_m}{n_{sync}} \tag{2.5}$$

The motor can be represented by an equivalent circuit of one phase of the machine (Figure 2.7), which allow to calculate some value analytically such as voltages, currents and torque in different section of the machine and for different operation conditions.
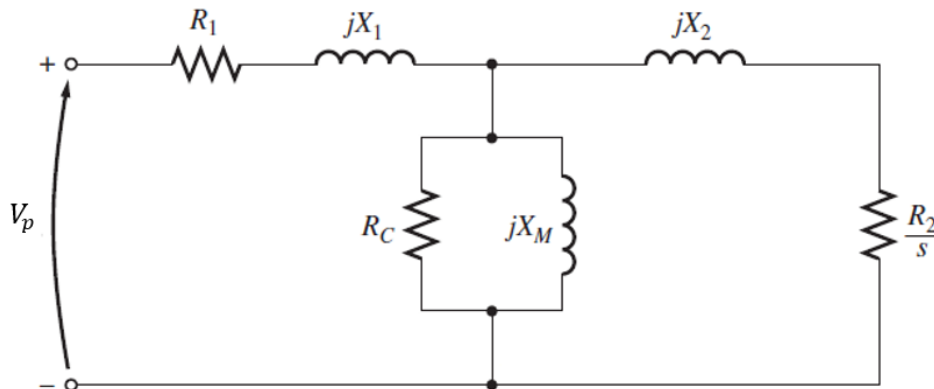
Figure 2.7 Induction motor equivalent circuit *(own source).*

In a first analytical study, mean torque values for different topologies of electric motors can be obtained, in the case of an induction motor, from the circuit illustrated in Figure 2.7, the induced mean torque developed by the machine can be obtained as shown in equation 2.6 [25].

$$T_{ind} = \frac{3V_{TH}R_2/s}{\omega_s\left[\left(R_{TH} + \frac{R_2}{s}\right)^2 + (X_{TH} + X_2)^2\right]} \tag{2.6}$$

Figure 2.8 shows the torque-speed characteristic curve for the motor and generator region in an induction machine.
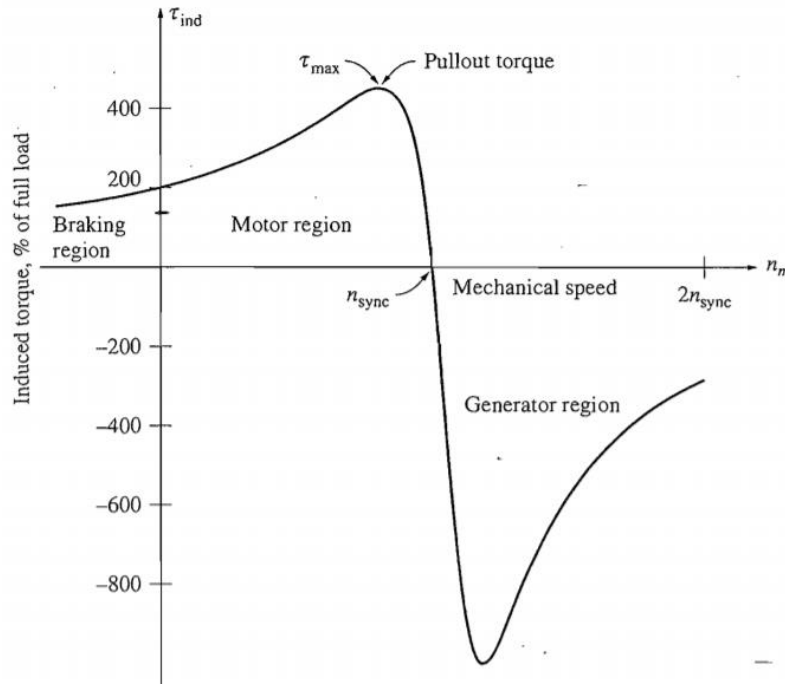
Figure 2.8 Induction motor torque-speed characteristic curve [25]**.**

2.2.3 Losses in induction motors

In the operation of an electrical machine there is a portion of the energy that is dissipated in the form of losses in the process. This is transformed into heat, therefore the calculation of the loss values is an important aspect in the thermal modeling of a motor, as discussed at the beginning of this chapter. Figure 2.9 illustrates a diagram of the powers and losses within an induction machine. The different sources of heat dissipation within a machine are summarized below.
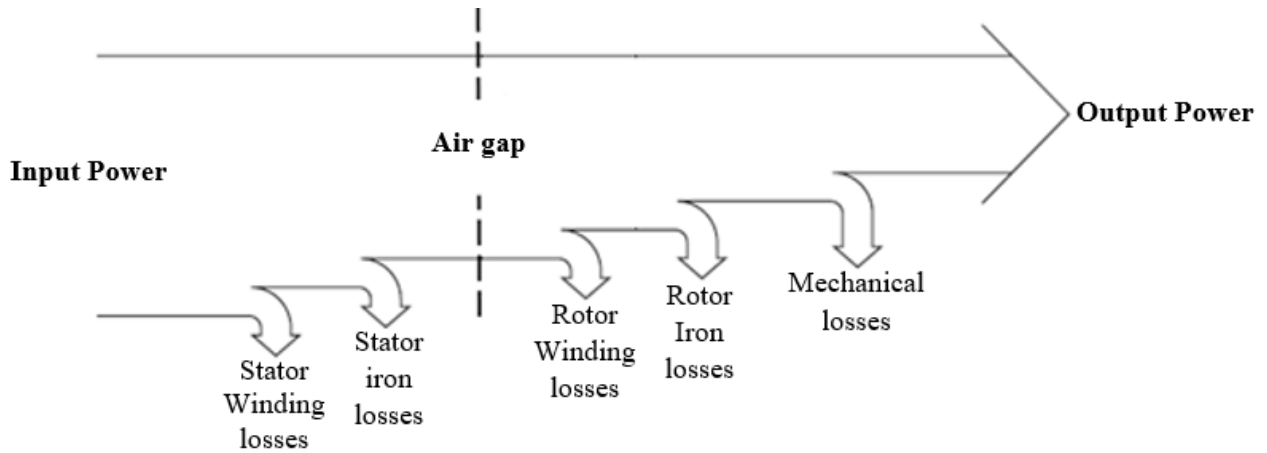
Figure 2.9 Diagram of the power losses in an induction motor *(own source)*.

- *Copper losses*

The circulation of current through the conductors in the coils and the rotor bars in an induction machine produces losses in the form of heat. This effect known as Joule losses, can be quantified as,

$$P_{joule} = R_{cond} \cdot I_{cond}^2 \tag{2.7}$$

In addition, the resistance of a conductor is given by the geometry and the type of material of it. That is to say,

$$R_{cond} = \rho \cdot \frac{l_{cond}}{A_{cond}} \tag{2.8}$$

The temperature also plays an important factor in the final value of the resistance of a conductor, where from the known base resistance, the final resistance of the material can be calculated as a variation in temperature. Equation 2.9 allows us to calculate this effect.

$$R_f = R_i \cdot (1 + \alpha \, \Delta T) \tag{2.9}$$

The coefficient α determines the increase or decrease of the electrical resistance according to the temperature variation and the nature of each material and can be determined experimentally.

- *Iron losses*

Iron losses can be classified into losses due to hysteresis (due to the magnetization and demagnetization cycles of the material), eddy current losses (due to the variation of magnetic flux observed by lamination) and excess losses (produced by wave deformations of the magnetic flux and imperfections in the material). The eddy currents can be decreased laminating the iron as shown in

figure 2.10. Due to the less surface area in the laminated sheets, the electrical resistances increase, diminishing the circulating currents and reducing the losses associated to this effect.

Solid core   Laminated core
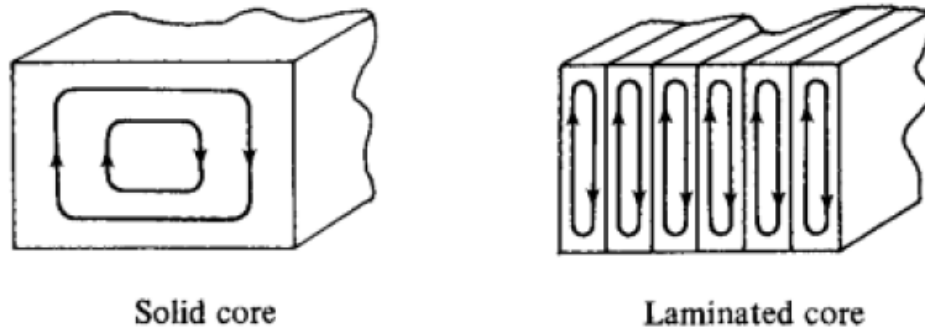
Figure 2.10 Representation of the iron lamination and the circulating currents [7]**.**

An analytical method to calculate the losses values is presented below [35]

$$P_{fe} = P_c + P_h + P_e \tag{2.10}$$

$$P_{fe} = k_h B_m^2 f + k_c B_m^2 f^2 + k_r B_m^{1.5} f^{1.5} \tag{2.11}$$

$$k_c = \frac{\pi^2 \sigma d^2}{6} \tag{2.12}$$

Where, σ is the material conductivity and d is the lamination thickness.

- *Mechanical losses*

In induction machines, the main sources of mechanical losses are the windage losses, ventilation losses and the friction losses mainly due to the bearings.

The bearing losses due to friction are related to the shaft speed, bearing type, lubricant type and the load on the bearing. According to [36] the bearing friction losses are

$$P_{bearing} = 0.5 \, \Omega \mu F \, D_{bearing} \tag{2.13}$$

Where, Ω is the angular frequency of the shaft, μ is the friction coefficient, F the bearing load and $D_{bearing}$ is the inner diameter of the bearing.

For the windage losses and ventilator losses, an experimental equation developed in [37] can be used to obtain this value as,

$$P_\rho = k_\rho D_r \left(l_r + 0.6\tau_p \right) v_r^2 \tag{2.14}$$

Where, k_ρ is an experimental factor (Table 2.3), D_r is the rotor diameter, l_r is the rotor length, τ_p is the pole pitch and v_r is the speed of the rotor. This equation is valid for normal speed machine.

Table 2.3 Experimental factors for bearing and windage losses

Cooling method	$k_\rho \ [W\,s^2/m^2]$
TEFC motors, small and medium size machines	15
Open-circuit cooling, small and medium sized machines	10
Large machines	8
Air-cooled turbogenerators	5

2.3 Heat transfer in electric machines

In electric motors, the heat transfer problem is one of the biggest concerns in the design process. The temperature can be the main reason of faults within the machine due to the premature aging of insulation, among other problems.
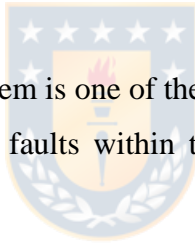
2.3.1 Conduction

The conduction is based in the heat energy transfer between two bodies that are touching each other, be they solid, liquid or gas. La heat distribution in a material can be described by the heat equation shown below,

$$\nabla \cdot (\nabla \Lambda \Theta) + q_h = \rho_m c_p \frac{\partial \Theta}{\partial t} \tag{2.15}$$

Where, Θ is the temperature, q_h is the heat generation rate, Λ is the thermal conductivity of the material, ρ_m is the density of the material and c_p is the specific heat. In steady state, eq. 2.15 can be written as,

$$\Lambda_x \frac{\partial^2 \Theta}{\partial x^2} + \Lambda_y \frac{\partial^2 \Theta}{\partial y^2} + \Lambda_z \frac{\partial^2 \Theta}{\partial z^2} = -q_h(x, y, z) \tag{2.16}$$

The thermal conductivity of materials is dependent of the temperature; in general, the conductivity in metals decrease with the rise of the temperature and with the insulating materials is the opposite case.

In electric machines, the material conductivity is an important aspect to considerate, because one of the main forms to evacuate the heat from inside a motor, is through conduction up to the housing, cooling the machine. Table 2.4 shows the thermal conductivity of materials often use in electric machines.

Table 2.4 Thermal conductivity of typical induction machine materials

Material	Thermal conductivity [W/Km]
Copper	400
Electric Steel	30-60
Aluminum	240
Conductor insulation	0.04-0.7
Slot liner	0.3

2.3.2 Convection

The convection is the conduction of heat from a body with greater temperature to a cooler fluid region because of the relative movement of the fluid with respect of the solid surface.

This phenomenon add complexity to the heat transfer model, because of the process nature that require a precise description of both the solid and the fluid coolant in terms of behavior, geometry and other parameters and experimental data to obtain satisfactory results. The heat transfer rate can be described by the Newton's Law of Cooling shown below,

$$\frac{dq}{dt} = h A_S (T_s - T_\infty) \tag{2.17}$$

Where h is the convection heat transfer coefficient, A_s is the surface area where the process occurs, T_s is the surface temperature and T_∞ is the fluid temperature far away from the surface (ambient temperature).

The convection process is a fundamental part in the thermal analysis of an electric machine. The most common cooling methods such as forced ventilation, self-ventilation or liquid cooling, take advantage of this phenomenon in addition of the conduction to evacuate the heat within the inside of the machine.

The heat transfer coefficient is one of the main parts of describing the process of convection in the induction machine model. For this purpose, a series of different dimensionless numbers were defined to reduce the variables and to explain certain characteristic of the interaction between a surface and the fluid.

First, we have the Prandtl number which indicates the momentum and heat dissipation rate in a fluid, defined as,

$$Pr = \frac{\mu C_p}{k} \tag{2.18}$$

The value of this number can tell a very quickly heat diffusion (Pr << 1) or a very slow one (Pr >> 1), a table of Prandtl numbers for common fluids is presented below,

Table 2.5 Prandtl number for common fluids

Fluid	Prandtl number
Gases	0.6 - 1
Water	7 - 14
Oils	50 – 100.000
Polymers	10.000

Before defining the next dimensionless number necessary for the convection process modeling, is convenient to introduce the concepts of laminar and turbulent flow. The first one is characterized by smooth streamlines and an ordered motion of the fluid particles. In the second case, there is highly

disorder motion of the particles and velocity fluctuation with the often presence of whirlpools. Figure 2.11 illustrates these two situations.
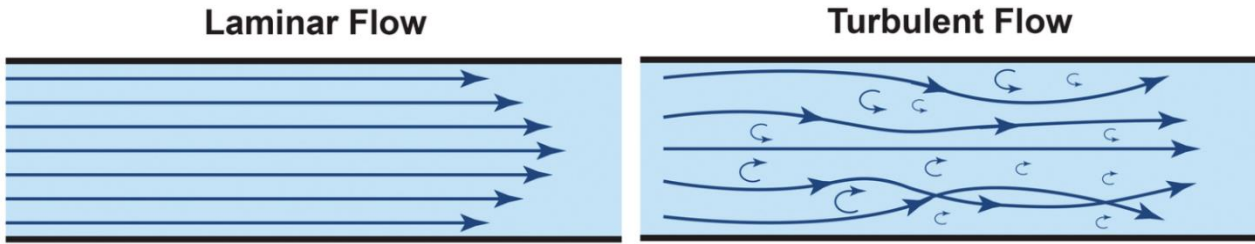
Figure 2.11 Laminar and turbulent flow representation [38]**.**

The Reynolds number represents the ratio between the inertia forces (proportional to the density and velocity) and the viscous forces (intrinsic property) in the fluid. This dimensionless value, can be represented as,

$$Re = \frac{\rho V L_c}{\mu_k} \tag{2.19}$$

Low values of this number indicate a laminar fluid behavior and large ones corresponds to turbulent flows. The transition between the laminar and turbulent cases is determined by the critical Reynolds number which varies with the geometry of the surfaces.

In the case of the natural convection process the Reynold number can't fully describe this phenomenon and the Grashof number is used. This value indicates the ratio of the buoyancy force to the viscous force acting on the fluid. The definition is shown below,

$$Gr = \frac{g\beta(T_s - T_\infty)L_c^3}{v^2} \tag{2.20}$$

The Grashof number provides the main criteria to determining whether the fluid flow is laminar or turbulent in natural convection (Such as the Reynolds number do it in the force convection case).

The Taylor number is closely related with the effects that occurs inside an electric machine. This value characterizes the instability of a fluid flow inside two differentially rotating concentric cylinders (such as the air in the airgap). This number is usually expressed as [39],

$$Ta = \frac{\Omega^2 r_m (r_2 - r_1)^3}{v^2} \tag{2.21}$$

And the modified Taylor numbers for not perfect cylindric geometries, can be calculated as shown below,

$$Ta_m = \frac{Ta}{F_g} \tag{2.22}$$

Where F_g, is defined as [39]

$$F_g = \frac{\pi^4 \left[\dfrac{2r - 2.304\delta}{2r - \delta}\right]}{1697 \left[0.056 + 0.0571 \left(\dfrac{2r - 2.304\delta}{2r - \delta}\right)^2\right][1 - 2r]^2} \tag{2.23}$$

Finally, the Nusselt number, which represents the enhancement of heat transfer through a fluid layer as a result of convection relative to conduction across the same fluid, is defined as

$$Nu = \frac{hL_C}{k} \tag{2.24}$$

As can be seen from equation 2.24, the Nusselt number is directly proportional with the heat transfer coefficient, but since we don't know any of these values, it cannot solve the problem. Becker an Kaye [39] develop a procedure to determine the Nusselt number from the modified Taylor number defined as,

$$Nu = \begin{cases} 2, & Ta_m < 1700 \\ 0.128 \cdot Ta_m^{0.367}, & 1700 < Ta_m < 10^4 \\ 0.409 \cdot Ta_m^{0.241}, & 10^4 < Ta_m < 10^7 \end{cases} \tag{2.25}$$

And so, with the Nusselt number obtained, the heat transfer coefficient can be calculated with equation 2.24.

2.3.3 Radiation

It is originated from the release of electromagnetic waves from a body into the space, which translate in a net energy loss and the cooling of the material. In contrast with conduction and convection, the radiation doesn't require a medium for the heat transfer effect to happen. The heat flux density is defined by the Stefan-Boltzmann equation.

$$q_{th} = \epsilon_{thr}\sigma_{SB}(T_1^4 - T_2^4) \tag{2.26}$$

Where T_1 and T_2 are the radiant and absorbent surface temperature respectably, σ_{SB} is the Stefan-Boltzmann constant and ϵ_{thr} is the relative emissivity between the two surfaces and is dependent of the material and relative position.

The emissivity property, with values between 0 and 1, is a measure of how closely a surface approximates a black body for which ϵ=1. Table 2.6 shows the emissivity for common materials.

Table 2.6 Emissivity of some motor common materials.

Material	Emissivity
Highly Polished aluminum	0.045
Cast iron	0.6-0.7
Copper (polished)	0.05
Black paint	0.9
Stainless steel	0.59

This heat transfer method has a relative low efficiency and is only significant when there are large temperature differences between the surface and the ambient. In electric machines plays a more important role when there is no cooling added to the machine and sometimes is neglected.

2.3.4 Lumped parameter model analysis

The prediction of the thermal behavior of an electric machine is one of the main parts in the design process. The calculation of the temperature distribution can give access to the necessary information to take decisions regarding the motor operation such as early fault diagnosis [40] or increase the power output of the equipment to improve performance.

The most used techniques and modern tools in the thermal modeling process associated with electric motor analysis require large amounts of computer power, time and experience from the user to give satisfactory results, so an easier and faster approach seems to be useful.

It turns out that the heat flow inside a body is analogous to the current flow running through conductors. Table 2.7 shows the similarities of these situations with the respective quantities.

Table 2.7 thermal and electricity analogies

Electric flow quantity	Symbol	Thermal flow quantity	Symbol
Electric current	I	Heat flow	Φ
Electric potential	V	Temperature	T
Electric conductivity	σ	Thermal conductivity	λ
Electric Resistance	R	Thermal resistance	R_{th}
Electric conductance	G	Thermal conductance	G_{th}
Capacitance	C	Heat capacity	C_{th}

The similarities detailed in table 2.7 indicates that a thermal circuit can be constructed to obtain the temperatures in different parts of the machine. Such as electrical circuit, the thermal circuit can be solved using equivalent laws and methods normally applied but adapted to this case. The losses of the motor are treated as current sources and the electric potential in each of the nodes correspond to the temperature in that place which are interconnected by the thermal resistances. The thermal capacitance is only use in the transient thermal state solution, but since in this work is only analyze the thermal steady state behavior of the machine, is not further investigated.

In order to build the thermal network to represent the induction machine and determine the temperature distribution, the resistances need to be calculated, but due to the nature of the heat transfer process, the properties and parameters are distributed along the volume of the bodies in the motor. For this purpose, the lumped parameter method is used to simplify the thermal model in which the mean temperature of the parts is obtained.

For example, a lumped parameter simplification of the tooth and the winding are presented in figure 2.12. In Figure 2.12b the copper losses are distributed along the winding and the resistances are calculated for infinitesimal lengths. In 2.12c the resistances parameter is concentrated in less nodes so the calculation would be simpler, and the temperature obtained are the mean ones for the copper and the tooth. Figure 2.12a shows the real component.
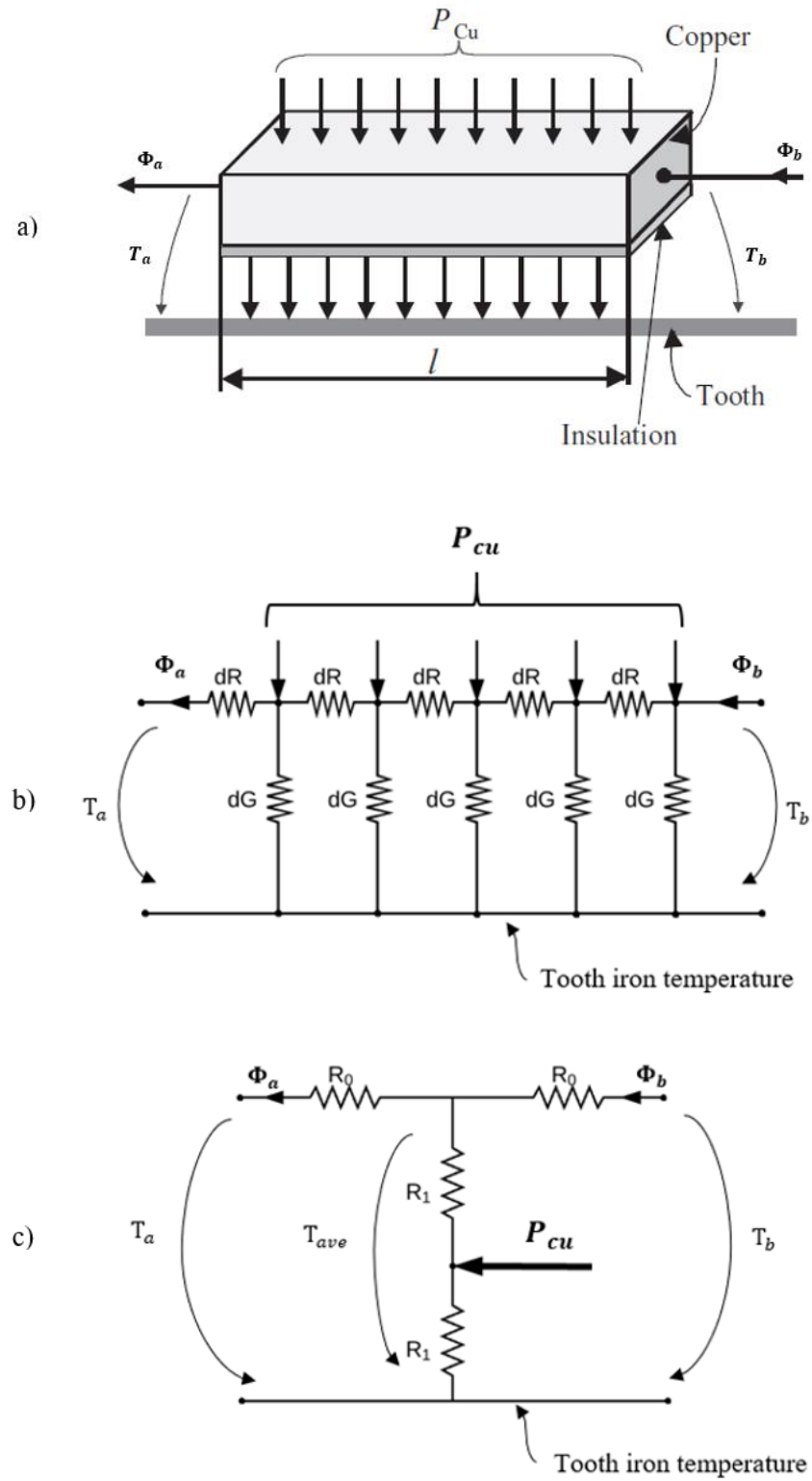
Figure 2.12 (a) Real component; (b) Thermal network presented with distributed parameters; and (c) the circuit with lumped constants [41]**.**

Finally, the assumptions of this method are listed below.

- The heat flow in the radial and axial direction are independent and thus do not influence each other.
- A mean temperature defines the heat flow both in the radial and axial directions.
- No circumferential heat flows.
- The heat generation is uniformly distributed along the bodies.

The electric resistance of a conductor can be obtained from its geometry and construction material as

$$R = \frac{l_{cond}}{\sigma \cdot S_{cond}} \tag{2.27}$$

By analogy, the thermal resistance of a plate (see figure 2.13) with thickness l and surface area S is defined as

$$R_{th} = \frac{l}{\lambda \cdot S} \tag{2.28}$$
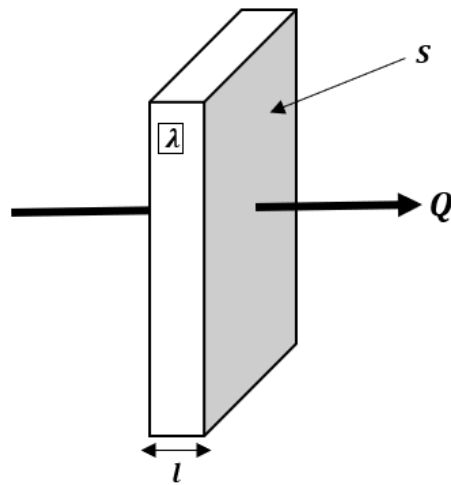
Figure 2.13 One-dimensional heat flow through a plate *(own source)*.

As seen in figure 2.13, the heat flow in one dimension is represented. Since is a rectangular plate, the thermal resistance of the body can be calculated with the same method in every direction. Although, a rectangular plate is a geometry that is found inside an electric motor, cylindrical components are also predominant in the construction of a machine. In this case the resistance is not equal in axial and

radial direction (see figure 2.14) and can be calculated by solving the heat flow equation in cylindrical form [42].
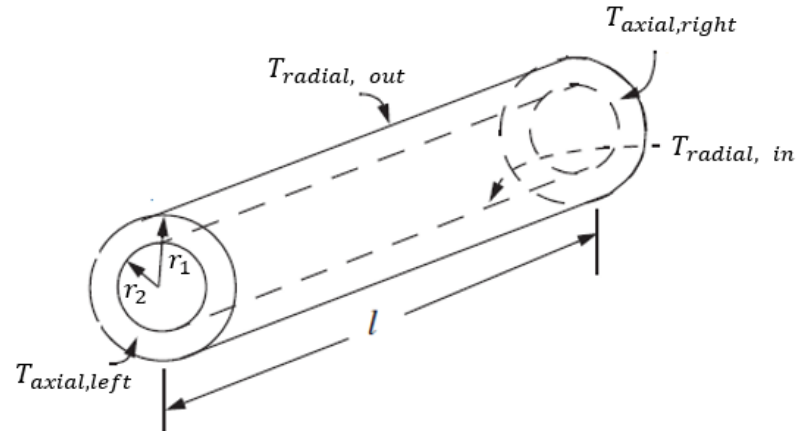
Figure 2.14 General cylindrical component *(own source)*.

As figure 2.14 show, the cylindrical component has more than one resistance and in order to obtain accurate results multiple elements need to be used to represent the body thermal parameters. Figure 2.15 is the network representing the cylinder including the heat flow in the radial and axial direction.
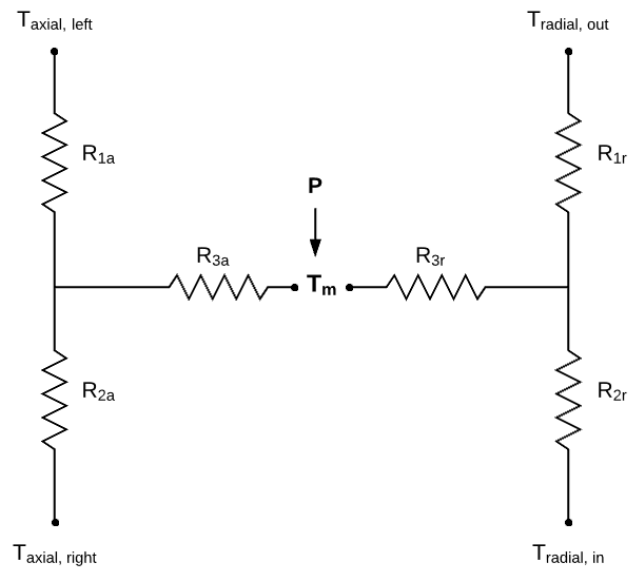
Figure 2.15 Thermal network representing the cylindrical component. T_m is the average temperature and the losses are denoted by P *(own source)*.

The two networks represent the radial and axial heat flow through the body and the central value T_m represents the average temperature of the cylinder. The nodes above and below each network represent the surface temperatures indicated in figure 2.14 and the resistances values can be calculated solving the one-dimensional conduction heat equation. The solutions for this case and for the other parts of an induction machine are detailed in annex A, based on the work of [39], [43]–[47].

A flow chart indicating the heat transfer process effect in each part of the motor is found in figure 2.16. Here, the interaction between each of the main components from the thermal perspective. The ambient air works as a reference node in the model where all the heat flow converge. The conduction process connects the stator iron, winding and the frame of the machine. In the rotor case, connects the lamination, the aluminum cage and the shaft. The airgap divides the motor in these two sections (stator and rotor), but the heat keeps flowing mainly through convection. These phenomena also appear in the interaction with the frame and shaft with the ambient and the stator and rotor end-winding with the end-space air of the motor. Finally, the radiation takes effect in in several components, but due to the relative low temperature operation inside an electric machine, can be neglected.

A simplified induction machine thermal network is presented in figure 2.17 where a 10-node circuit needs to be solved in order to find the temperature distribution. The reference node is the ambient temperature, and the voltage drop across any of the resistance represents the temperature change. The current sources indicate the losses injection in some of the nodes which are detailed in table 2.8. In following sections, the thermal circuit for each component would be described and a complete network would be illustrated.
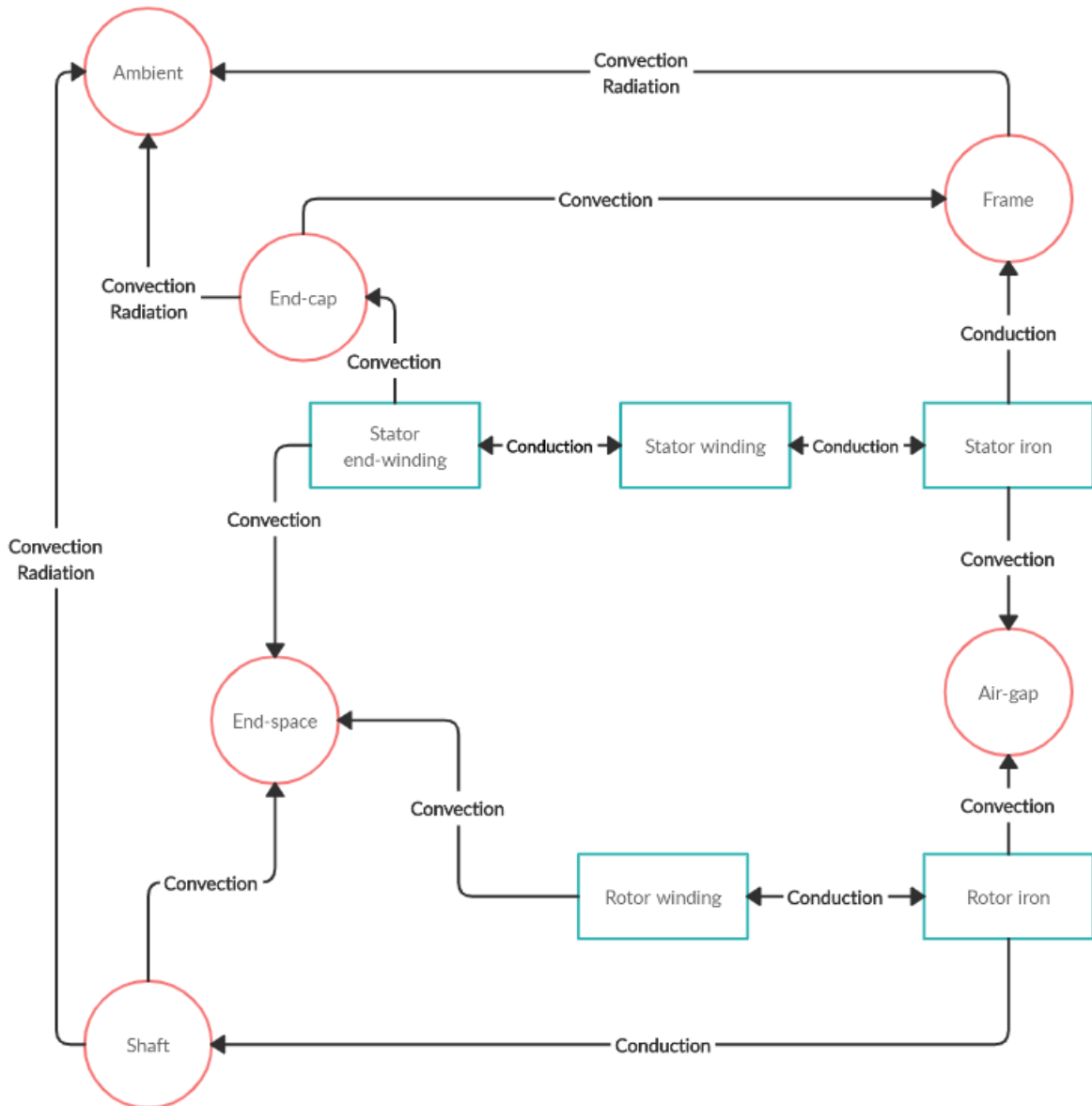
Figure 2.16 Flow chart showing the heat transfer relationship between the motor parts *(own source).*
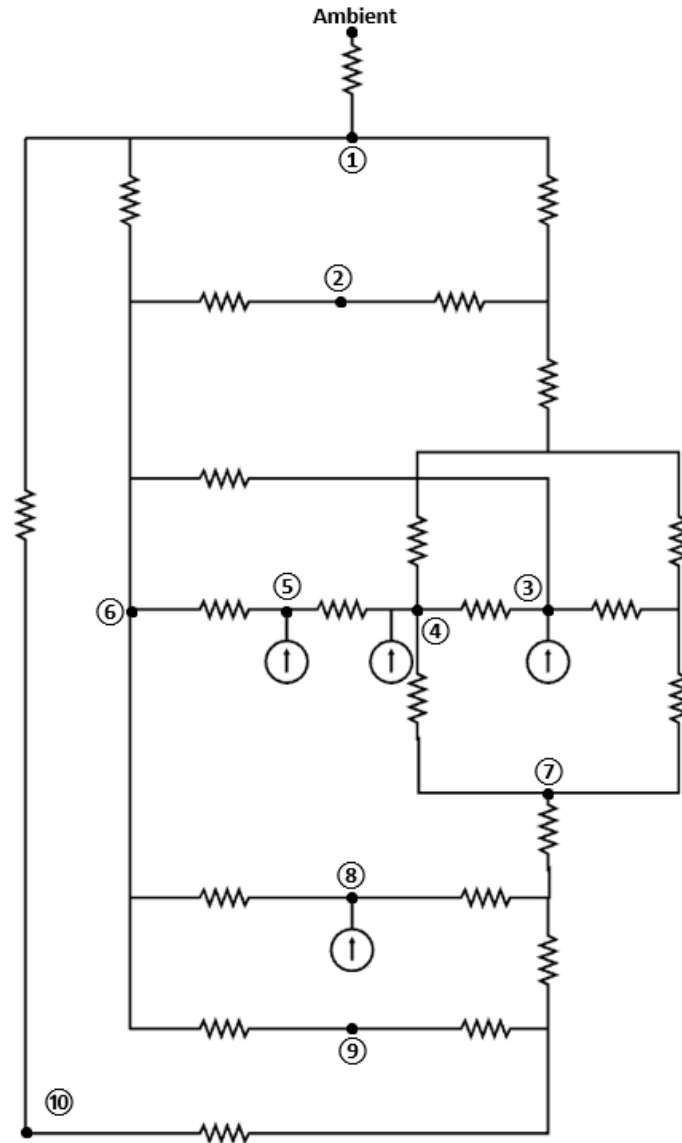
Figure 2.17 Induction motor thermal network *(own source)*.

Table 2.8 Nodes description in figure 2.9 thermal network.

Node number	Description	Node number	Description
1	Frame	6	End cap air
2	Stator iron	7	Air gap
3	Stator teeth	8	Rotor winding
4	Stator winding	9	Rotor iron
5	End winding	10	Shaft

To solve the circuit and obtain the node voltages, the conductance matrix method is used as it is done in the electric case. For the steady state solution, the temperature in each node is given by,

$$T = G^{-1}P + T_{amb} \tag{2.29}$$

Where, P is a vector containing the losses in each node. T is the temperature vector and, T_{amb} is the ambient temperature vector. Finally, the resistances in the circuit are used to build the $n \times n$ conductance matrix G, where n is the number of nodes in the network. This conductance matrix is defined as

$$G = \begin{bmatrix} \sum_{i=1}^{n} \dfrac{1}{R_{1,i}} & -\dfrac{1}{R_{1,2}} & \cdots & -\dfrac{1}{R_{1,n}} \\ -\dfrac{1}{R_{2,1}} & \sum_{i=1}^{n} \dfrac{1}{R_{2,i}} & \cdots & -\dfrac{1}{R_{2,n}} \\ \vdots & \vdots & \ddots & \vdots \\ -\dfrac{1}{R_{n,1}} & -\dfrac{1}{R_{n,2}} & \cdots & \sum_{i=1}^{n} \dfrac{1}{R_{n,1}} \end{bmatrix} \tag{2.30}$$

Where the diagonal elements are the sum of the conductance (inverse of the resistances) connected to the node n, and the element $G(i,j)$ is the thermal conductance connecting the nodes i and j with a minus sign.

In recent years, some research has been done in this matter. In [48], a reduced lumped parameter thermal network for an induction motor is built to analyze the effect of harmonic grid in the temperature of the machine. This reduction is done to minimize the time and computer efforts and the results shows good accuracy compare to a full network. Also, in [49] an artificial element is added to the multiphysics modeling process, where an artificial neural network is used to estimate certain parameters of the IM and then these results are the input data for the LPM thermal network.

A lumped parameter thermal model for other machines beside the induction motor has also been developed. A LPM thermal model for a synchronous reluctance motor is developed in [50]. This network shares several similarities with the one developed in this thesis, with some differences in the rotor component. The work done in [51] shows a thermal model built for a permanent magnet motor. This study has been getting more attention lately, due to the recent development in magnetic materials

and the applications in the electromotive industry. Finally, in [52] and [53] an axial flux permanent magnet machine thermal model was constructed using this technique. This topology in electric motor has been gaining more attention due to advantages in power density, efficiency and size in comparison with standard machines.

2.4   Multiphysics analysis and Numerical software

Due to the complexity of an electric machine, a multiphysics approach is necessary to ensure an accurate and correct design or analysis because of the multiple number of phenomena interacting with each other that affect the results of the calculations.

2.4.1 Multiphysics design workflow

This process starts with stablishing the design requirements (as shown in figure 2.18), where the application and the dimensioning of the machine parts are defined, and may include other parameters such as, speed, torque, efficiency, etc. In this stage, different design procedures are used using analytical and optimization techniques having certain restrictions depending de final application [54].

The second step is the electromagnetic analysis. Usually with the aid of a software, the engineer is capable to simulate the behavior of the machine previously designed, obtaining certain results, like electromagnetic torque, forces, winding and iron losses inside the motor, efficiency and the general performance of the drive (from the electromagnetic standpoint). These results can be obtained from an analytical or numerical procedure, often aided by computer software.
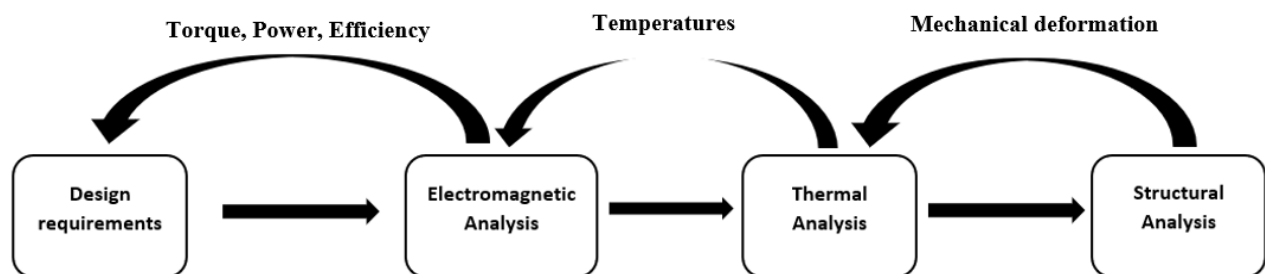
Figure 2.18 Multiphysics design workflow *(own source).*

The thermal analysis uses the losses calculated in the electromagnetic study as inputs to determine the temperature distribution inside the machine. These results are obtained by solving the heat transfer equation reviewed in chapter 2.3, often with the help of a computer software. The number of simplifications made to the model would define the complexity and the amount of time needed to reach a satisfactory solution. These simplifications vary from changing the geometry (eliminating or changing certain parts of the machine) or neglecting the radiation or convection effect in certain cases. All this would depend in the user experience.

The last step of this process is the structural analysis, where with the information of the magnetic forces obtained from the electromagnetic analysis and the temperatures distribution data from the thermal study, a stress and deformation analysis, noise vibration and structural dynamics analysis could be carried out.

This design process has an iterative nature. In each step of the development of the machine, if some requirement is not achieved, then the user can go to one of the previous steps to adjust some values or change the parameters of the motor. Because of this, the entire process could take a large amount of time, so the simplification mentioned before may be necessary to accelerate the work if the results meet the precision criteria of the designer.

An electric machine could be studied from a more general perspective besides its operation. In [55] a lifecycle of a motor study is carried out, where besides the design process already mentioned, the manufacturing, use phase and recycling part is taking account, as shown in figure 2.19. This approach may optimize the machine performance further, and with modern tools available, the design and production of a motor could be more profitable in the long term. This is a very relevant feature in modern manufacturing industry due to the several social, economic and environmental benefits of the circular economy associated to this process [56].
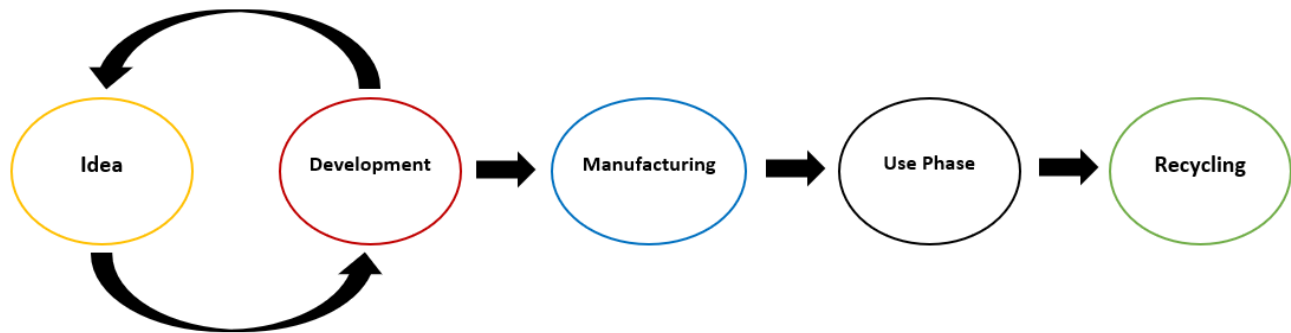
Figure 2.19 Lifecycle of an electric machine *(own source)*.

2.4.2 Finite element analysis (FEA)

In the design or analysis process of an electric machine, it is necessary to solve the differential equations governing the electromagnetic, thermal and other phenomena. Due to the complexity of the geometry and the amount of parts and external conditions that the user must account, the aid of a computer software becomes a necessity to obtain satisfactory results.

The finite element analysis software is one of the tools that a designer can use to simulate the behavior of the machine. This method is used mainly in the electromagnetic and structural analysis and with some assumptions, the thermal analysis also can be carried out.

The FEA method consist in the subdivision of the complete domain of study in smaller parts called finite elements. Then, in each of these sections, the method solves approximated forms of the differential equations and imposing continuity between the elements to ensure valid results. The subdivision of the domain is called mesh, and smaller elements translates in more accurate resolves, but mean longer compute times [57].

2.5 Summary

In this chapter, a review about the most important topics related to this thesis was done.

First, a brief introduction about material selection was carried out regarding those that are used in induction machines. The characteristics and behavior of soft and hard magnetic materials are discussed, which are the main component in the magnetic circuit of the motor. Also, other materials involving different parts of the motor are commented.

Then, the basics of the electromagnetic analysis are introduced. The forces and torque production mechanism, such as the Lorentz force is described. Due to the nature of the studied motor, the induction machine principles are also discussed, where the electric circuit is presented, and the torque-speed characteristic curve is presented among other features. Then, the losses components in an electric machine (copper, iron and mechanical) are introduced and described mathematically, since these values are the input data for the thermal analysis done afterwards.

Since the thesis is focused in the thermal analysis of an induction motor, a review of this topic was needed. First, the principle of the heat transfer phenomena is introduced, where conduction, convection and radiation are described and the equation governing its behavior are shown. Later, the lumped parameter method is introduced as a procedure to build a thermal network that represents the induction motor and find the temperature distribution within it. The circuit is solve using analogous methods and equation applied in the electric case and adapted for this purpose. A complete network representing the test motor is presented and the procedure to solve this problem is addressed.

Finally, the topic regarding the electric machine design workflow is studied. From the first idea for a prototype to the design process involving the electromagnetic, thermal and structural analysis, and even commenting the rest of an electric motor lifecycle. Then a brief description of the numerical method used in this thesis is mentioned.

Chapter 3.   Electromagnetic analysis

3.1   Machine description

The machine analyzed in this thesis is an induction motor. The particularity of this machines is the iron material with which it has been built. It is a M800-65A electrical steel which have high losses in comparison with other lamination in standards motors. This material was selected to visualize the eddy current losses and the temperature distribution more easily to simplify the thermal model creation process. Some parameters and rated values are summarized in table 3.1.

Table 3.1 Induction machine parameters and rated values

Parameter	Value	Unit
Axial length	160	mm
Stator outer diameter	220	mm
Rotor outer diameter	124	mm
Air gap	0.5	mm
Skew angle	8.5	Degrees
Rated voltage	400	V
Rated frequency	50	Hz
Rated power	5	kW
Rated speed	1467	min^{-1}
Rated current	10.4	A

About the geometry, it is a standard induction motor with the exception that it does not have a fan mounted in the shaft. The stator and rotor slot geometry of the machine are illustrated in figure 3.1 and the main dimension of the motor are shown in figure B.1 in annex B.
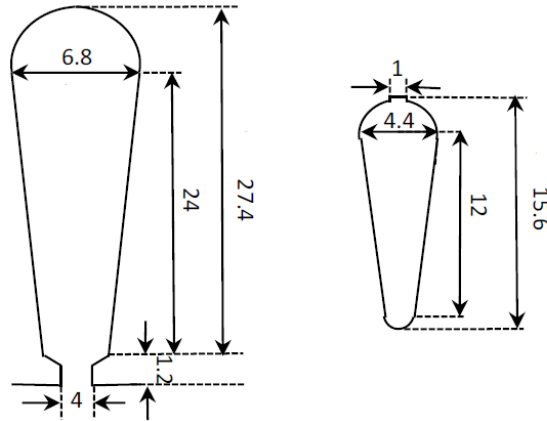
Figure 3.1 Stator (left) and rotor (right) slot geometries and dimensions [58]**.**

The motor has a single layer winding shown in figure 3.2. the layout only shows 12 slots due to the symmetry of the machine (see figure 3.3). In the figure, the cross symbolizes the current entering the winding and the circle symbolize the current exiting the winding.
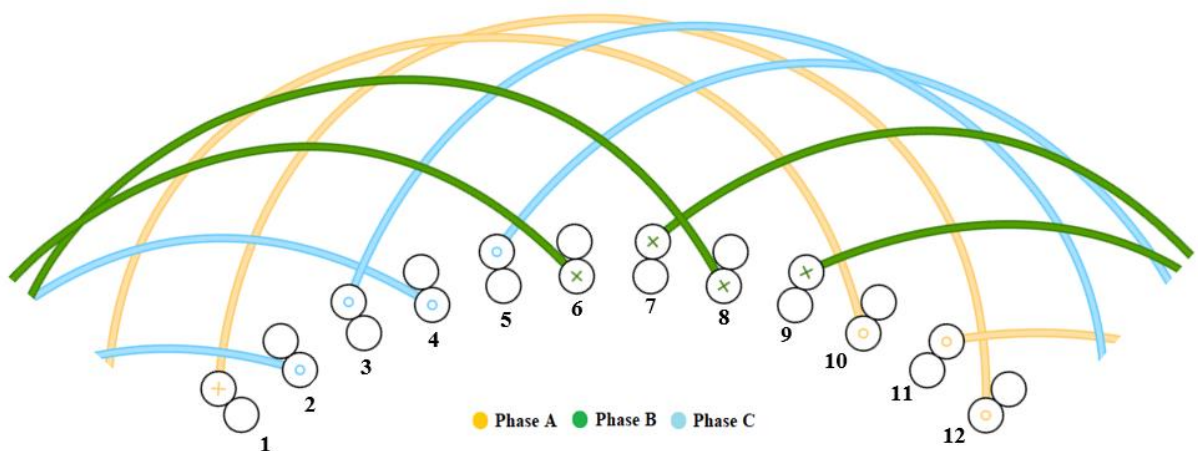
Figure 3.2 Induction machine winding layout *(own source)***.**

3.2 Electromagnetic modeling

The electromagnetic analysis of the induction machine was carried out with a finite element analysis software, where a different number of simulations were made to obtain some results of interest.

The first step is defining the geometry, and the boundary conditions in the model. For this analysis, a 2-D representation of the motor was used to reduce the complexity and the computation time. Also,

only 1/4 of the machine was modeled due to the symmetry and periodicity properties of magnetic field solutions. Figure 3.3 shows the geometry use to the electromagnetic simulations.
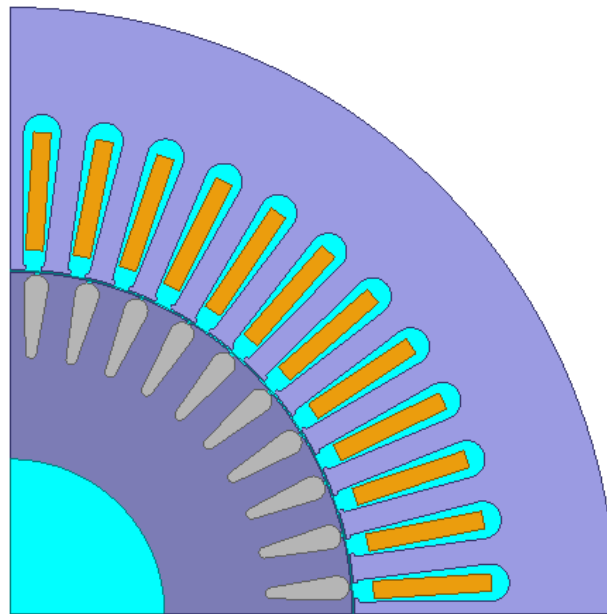
Figure 3.3 Model of the induction motor for the electromagnetic simulations *(own source)***.**

The material definition is another important point in the electromagnetic modeling of the electric machine. Figure 3.4 shows the B-H curve of the electrical steel used in the simulations. The frame and the shaft are not included in the simulations because the structural steel have a magnetic permeability close to the one of the vacuum.
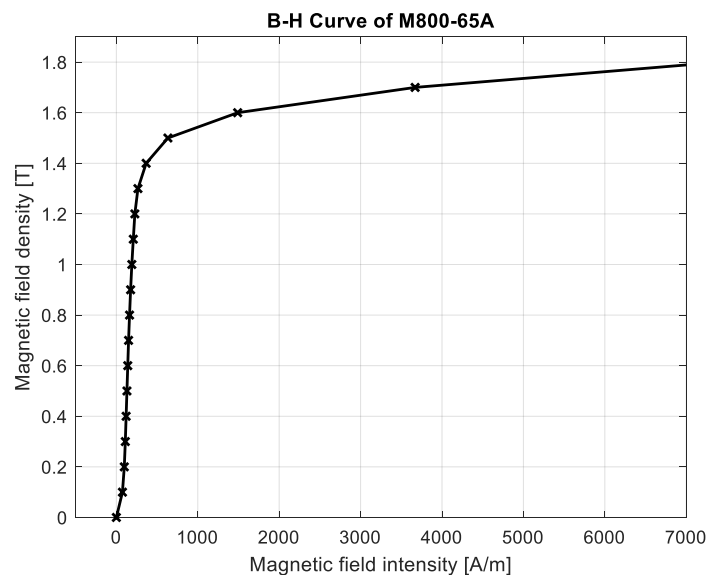
Figure 3.4 B-H curve of the steel M800-65A *(own source).*

3.3 Losses calculations

The Joule losses of the stator copper and the rotor cage are carried out. An analytical method is used base on the works in [58], [59].

The stator winding losses are obtained from the equation 2.13. Since the test subject is a small motor, the AC effect on the resistance can be neglected, so the DC value of the parameter is

$$R_s = \frac{l_{cu}}{\sigma_{cu}S_{cu}} \tag{3.1}$$

Where, l_{cu} is the total length of the copper, S_{cu} is the cross-sectional area of one conductor in the slot. σ_{cu} is the conductivity of the copper material, but the estimated working temperature must be considered. Thus, the conductivity for a specific temperature is calculated as

$$\sigma_{cu} = \frac{\sigma_{cu,ref}}{1 + \alpha_{cu}T_s} \tag{3.2}$$

Where, $\sigma_{cu,ref}$ is a known conductivity value of the copper for a reference temperature, α_{cu} is the temperature coefficient of the material and T_s is the estimated temperature rise of the winding from the reference one.

For the rotor cage losses, the same method of the stator losses can be applied, then

$$P_{rot} = 3 R_r' (I_r')^2 \tag{3.3}$$

Where, R_r' is the rotor resistance and I_r' is the current of the rotor part in the equivalent circuit referred to the stator (which can be obtained solving the electrical network presented in figure 2.7 for a certain operation pint). As we did with the stator winding, the rotor bar resistance can be calculated as

$$R_{bar} = \frac{l_{bar}}{\sigma_{Al}S_{bar}} \tag{3.4}$$

Where, l_{bar} is the rotor bar length, σ_{Al} is the conductivity of the aluminum and S_{bar} is the cross-sectional area of the rotor bar. The rotor cage end ring must be also considered, so the resistance of this element can be calculated as

$$R_{ring} = \frac{l_{ring}}{\sigma_{Al}S_{ring}} \tag{3.5}$$

Due to the geometry of the cage, the length of the ring associated to one bar is

$$l_{ring} = \frac{\pi D_{ring}}{Q_r} \tag{3.6}$$

Where, D_{ring} is the average diameter of the ring and Q_r is the number of the rotor slots. Finally, the rotor resistance can be calculated as [60]

$$R_r = R_{bar} + \frac{R_{ring}}{2\left(\sin\left(\frac{\pi p}{Q_r}\right)\right)^2} \tag{3.7}$$

Where the argument of the sine function represents the angular shift of the bar currents. The resistances and losses calculated are presented in table 3.2.

The iron losses are calculated with the same method used by the FEA software. For this purpose, the losses per weight data provided by the manufacturer (table B.2 in annex B), and other electrical steel data are used to obtain the coefficients. As previous stated, the total iron loss in the steel core are

$$P_{fe} = P_h + P_c + P_e = K_1 B_m^2 + K_2 B_m^{1.5} \tag{3.8}$$

Where P_h represents the hysteresis losses, P_c the classical eddy current losses, P_e the excess losses and B_m is the maximum flux density in the core at the operation point (obtained from finite element analysis or analytical results). The losses can be calculated as

$$P_h = k_h \, f \, B_m^2 \tag{3.9}$$
$$P_c = k_c \, f^2 \, B_m^2 \tag{3.10}$$
$$P_e = k_e \, f^{1.5} \, B_m^{1.5} \tag{3.11}$$

And therefore

$$K_1 = k_h f + k_c f^2 \tag{3.12}$$
$$K_2 = k_e f^{1.5} \tag{3.13}$$

The main goal is to obtain the k_h, k_c and k_e coefficients. The classical eddy current loss coefficient can be obtained directly as [61]

$$k_c = \pi^2 \sigma \frac{d^2}{6} \tag{3.14}$$

Where σ is the steel conductivity and d is the thickness of the lamination sheets. To obtain the remaining coefficients, the algorithm tries to fit equation 3.8 into the curve built from the losses characteristic curve data provided by the manufacturer. This is done by minimizing the quadratic error of the difference between the losses known data with the polynomial form. In this case we have

$$err(K_1, K_2) = \sum_i \left[p_{vi} - \left(K_1 B_{mi}^2 + K_2 B_{mi}^{1.5} \right) \right]^2 = min \tag{3.15}$$

Where, p_{vi} and B_{mi} are the i-th point of the data on the loss characteristic curve. One we obtain the values for K_1 and K_2, the remaining coefficient can be calculated as

$$k_h = \frac{K_1 - k_c f_0^2}{f_0} \tag{3.16}$$

$$k_e = \frac{K_2}{f_0^{1.5}} \tag{3.17}$$

Where, f_0 is the operating point frequency. Finally, the losses in the induction motor are summarize in the table below.

Table 3.2 Resistances and losses distribution inside the IM

Variable	Values
Stator resistance	0.534 Ω
Rotor resistance	0.630 Ω
Stator Joule losses	162 W
Rotor Joule losses	132 W
Iron losses	205 W

At the beginning of this section, one of the reasoning behind the electrical steel choice for the stator and iron core, was the high losses associated to the material, so to point out the importance of the material selection into the design process, a comparison was made between the used electrical steel (M800-65A), a medium losses one (M470-50A) and a low losses steel (M250-35A) from the same manufacturer. The exact same procedure is used to obtain the coefficient for the others (power

characteristic curve data in annex B) and the results of the losses distribution are shown in figure 3.5. Table 3.3 shows the coefficient values in each case.

Table 3.3 Coefficients values for the three electrical steel.

Electrical Steel	k_h	k_c	k_e
M250-35A	119.21	0.37	3.18
M470-50A	176.18	1.25	8.63
M800-65A	227.26	2.80	17.01
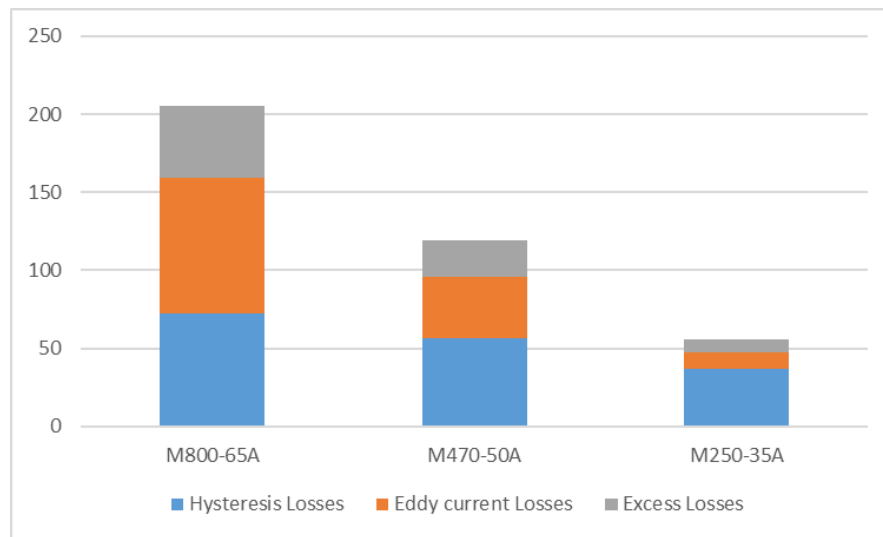
Figure 3.5 Iron Losses distribution for each Electrical steel *(own source)*.

3.4 Conclusions

In this chapter, the electromagnetic analysis of the induction motor was carried out. The study was centered in the loss distribution of the machine, because these values are the input data for the heat transfer analysis, which is the main goal of this thesis.

From the results derived by this study, it is clear that the material selection plays an important role in the design process of an electric machine. From figure 3.5, the total losses produced by the M250-35A is only 25% with respect to the M800-65A material, and the eddy current losses are the ones that vary the most, representing more of 40% of the total value in the actual material and less than 20% with the low loss steel mainly due to the lamination thickness variation between the sheets (0.65mm

for the M800-65A and 0.35mm for the M250-35A) and this difference allows a better visualization of each loss component.

Regarding the stator copper losses, these are usually the predominant component in an electric machine due to their variation with the square of the current, but since the choice for a lower grade steel, would translate in a higher estimate temperature, the resistance increases and thus, the overall machine temperature increases further. The Joule rotor losses can be difficult to obtain analytically due to the geometry of the bars and the end-ring. Because is manufactured only with aluminum no insulation and short-circuited on the ends, this is a major loss source for the machine and one of the hottest spots in the motor.

It is important to indicate that a complete electromagnetic analysis does not focus only in the loss calculation and distribution in the electric machine. The torque profile, electrical and mechanical power, magnetic flux density analysis, currents, and harmonic studies are also very important characteristics in the design workflow. However, since the goal of the thesis is centered in the thermal behavior of the motor, the losses, which are the input data for the heat transfer analysis, are mainly reported in this chapter.

Chapter 4.   Thermal analysis

4.1   Lumped parameter model results

In this section, the temperature distribution of the induction motor due to the solution of the thermal network is presented. In figure A.1 in annex A, the final thermal circuit is illustrated, with all the resistance considered in the solution and the corresponding nodes. In table 4.1 a description of each of the resistances is presented. In Annex C, the parameters used to calculate the resistances values and the Matlab script associated are presented.

Once the thermal network resistances are obtained, in order to solve equation 2.31, the conductance attached to each node are necessary to build the matrix involved in the calculations. Based on the resistances described in table A.1 in annex, some of the conductance are,

$$g_{12} = \frac{1}{R2 + R4 + R5} \tag{4.1}$$

$$g_{17} = \frac{1}{R22} \tag{4.2}$$

$$g_{110} = \frac{1}{R37} \tag{4.3}$$

$$g_{11} = g_{12} + g_{17} + g_{110} + \frac{1}{R1} \tag{4.4}$$

Where, g_{11} is the first eleement in the main diagonal of the conductance matrix and is the sums of all the conductance connected to node 1. g_{12}, g_{17} and g_{110} are the inverse of the resistance connected between node 1 and node 2, 7 and 10 respectively. The rest of the matrix elements are found with the same procedure. Finally, the matrix is shown below,

$$
G = \begin{pmatrix}
g_{11} & -g_{12} & 0 & 0 & 0 & 0 & -g_{17} & 0 & 0 & -g_{110} \\
-g_{12} & g_{22} & -g_{23} & -g_{24} & 0 & 0 & -g_{27} & 0 & 0 & 0 \\
0 & -g_{23} & g_{33} & -g_{34} & -g_{35} & 0 & -g_{37} & 0 & 0 & 0 \\
0 & -g_{24} & -g_{34} & g_{44} & -g_{45} & -g_{46} & 0 & 0 & 0 & 0 \\
0 & 0 & -g_{35} & -g_{45} & g_{55} & 0 & 0 & -g_{58} & 0 & 0 \\
0 & 0 & 0 & -g_{46} & 0 & g_{66} & -g_{67} & 0 & 0 & 0 \\
-g_{17} & -g_{27} & -g_{37} & 0 & 0 & -g_{67} & g_{77} & -g_{78} & -g_{79} & 0 \\
0 & 0 & 0 & 0 & -g_{58} & 0 & -g_{78} & g_{88} & -g_{89} & 0 \\
0 & 0 & 0 & 0 & 0 & 0 & -g_{79} & -g_{89} & g_{99} & -g_{910} \\
-g_{110} & 0 & 0 & 0 & 0 & 0 & 0 & 0 & -g_{910} & g_{1010}
\end{pmatrix}
$$

Then, the ambient temperature is set to 31.7 °C (experimental data) and the power losses vector considered five heat injection nodes which are shown below

$$
P = \begin{pmatrix}
0 \\
\dfrac{P_{fe,yoke}}{2} \\
\dfrac{P_{fe,teeth}}{2} \\
\dfrac{P_{cu}}{4} \\
0 \\
\dfrac{P_{cu}}{4} \\
0 \\
\dfrac{P_{Al}}{2} \\
0 \\
0
\end{pmatrix}
$$

Where, $P_{fe,yoke}$ are the losses in the stator yoke, $P_{fe,teeth}$ are the losses in the stator teeth, P_{cu} are the stator winding losses and P_{Al} are the rotor squirrel cage losses. The stator iron losses are assumed to be uniformly distributed between the yoke and the teeth. The same situation is considered between the copper slot portion and the end-winding. The rotor iron losses are neglected due to the low frequency of the circulating currents.

Finally, the temperature distribution is shown in figure 4.1. The temperature variation in each node is calculated and with an ambient temperature of 31.7 °C. The temperature values are obtained considering the coupling of the electromagnetic and thermal models (this is more detailed in a

following section). The maximum temperature calculated is in the rotor winding (which is expected for induction motors), reaching 125°C. In annex B, table B.3 the detail of the temperature for each part are presented. One of the critical parts to analyze regarding the thermal results are the stator windings. The thermal network solution shows that the average temperature in the stator slot is 97 °C, so according to table 4.1 the maximum temperature allowed by an insulation class A is greater than the temperature calculated but since is an average value, the winding could be at the limit operating point.

Table 4.1 Insulation class temperature information

Insulation Class	Maximum average temperature rise (°C)	Maximum winding temperature (°C)
A	60	105
B	80	130
F	105	155
H	125	180
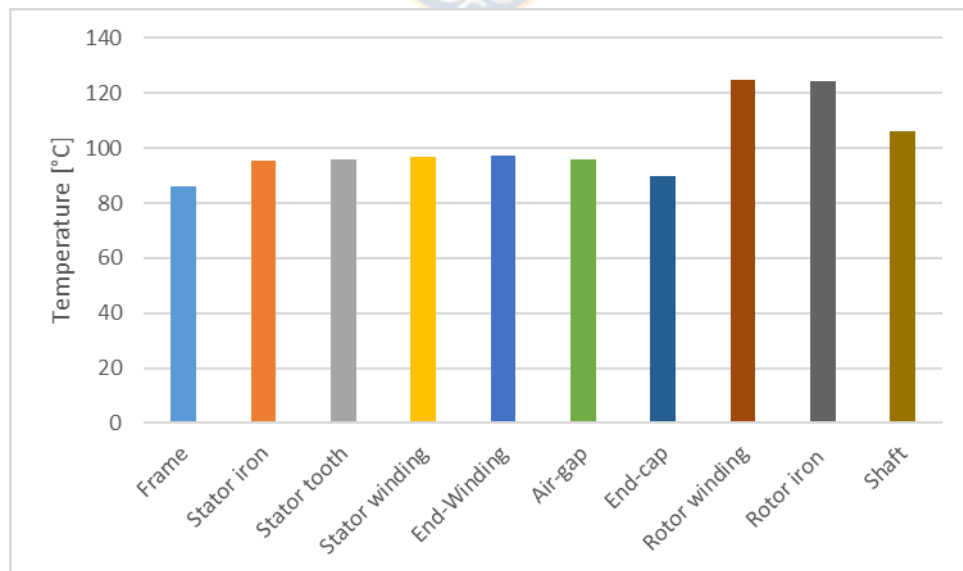
Figure 4.1 Temperature distribution inside the induction motor *(own source).*

A sensitivity analysis of the thermal network was also carried out. With this study, the temperature variation can be estimated when some of the parameters or the electric machine materials are change. First, the change of the housing surface is studied. This can be interpreted as the addition or reduction of the numbers of fins in the frame. Figure 4.2 shows the temperature distribution of the machine for these situations. As expected, the increase of surface in the frame of the motor facilitates the convection heat transfer between the machine and the ambient. For the case in which the surface area was reduce a 20% with respect to the original value there was an average increase of 9% in the temperatures, where the stator components were the more affected parts. In the other case (20% increase in the surface area) in average, the temperatures were about 8% lower in the machine.
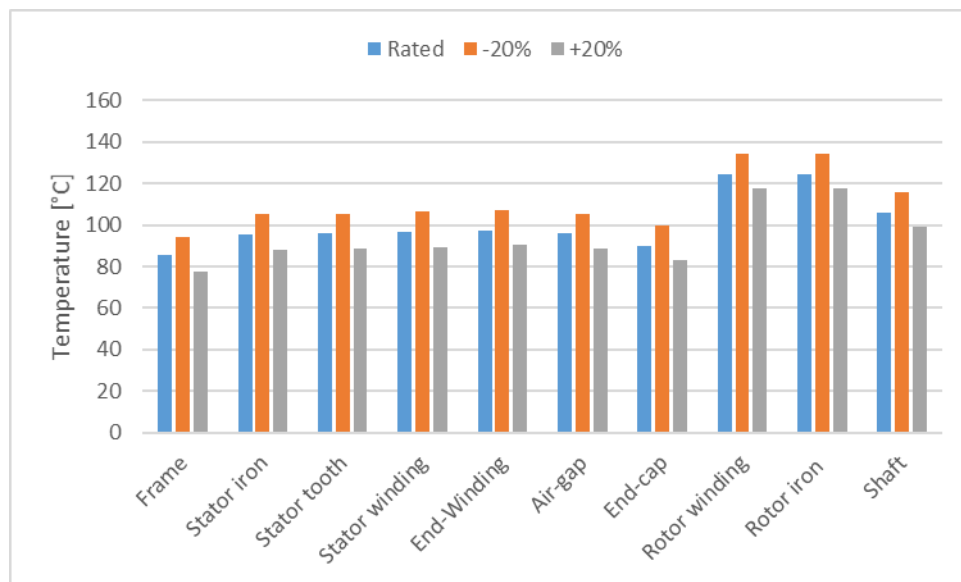
Figure 4.2 Temperature variation in each part of the IM with the change of the housing surface *(own source)*.

Other studied case was the change of the shaft material to observe the incidence of the thermal conductivity in the heat transfer process in this machine. The original material of the shaft is mild steel, and other two component were considered base on the usual alloys used in the manufacturing of this part. Carbon steel use in small motors and Nickel Chromium Molybdenum (NCM) alloy for heavy duty applications were used in the calculation with 60 W/mK and 10 W/mK for thermal conductivity respectively. Figure 4.3 shows the results and the comparison between the different cases. Since the material change was studied in the shaft, is expected to find that the stator was barely affected in both situations. On the other side, the rotor iron and rotor winding, which are in direct contact with the shaft, saw a 5% temperature reduction with the carbon steel material and a 12%

temperature increase with the NCM material. These results show the big difference that the material selection can have in the design process, always considering various factors concerning the performance of the motor, such as structural behavior and cost restrictions, among others.
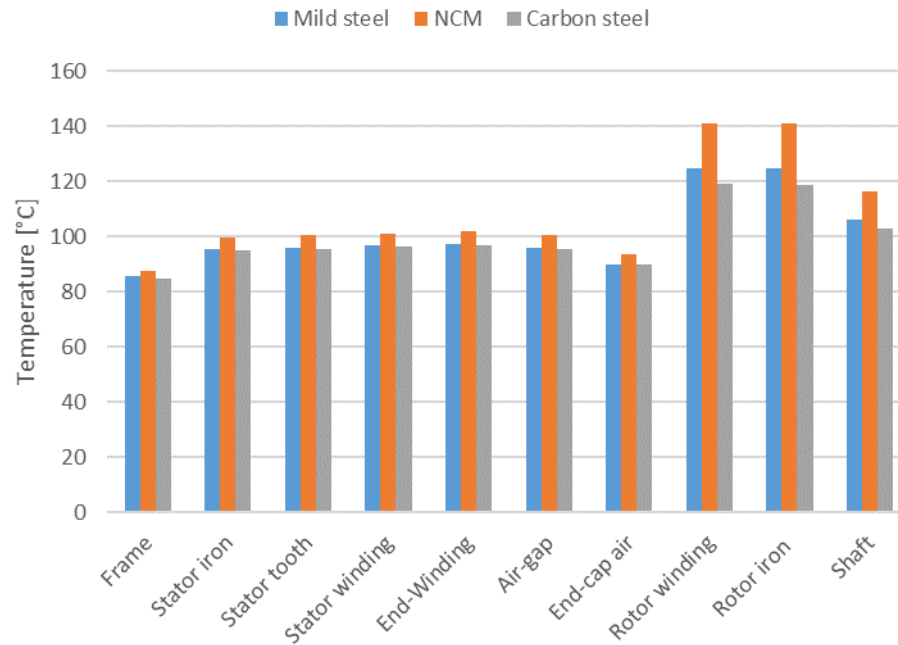
Figure 4.3 Temperature variation with the change of the shaft material selection *(own source)***.**

One final case was analyzed regarding the sensitivity study. In the electromagnetic analysis chapter, a comparison between the electrical steel M800-65A and other laminations with better performance was made from the iron losses standpoint. The results showed large differences from the material choice. Figure 4.4 illustrate the temperature difference for the three cases. The temperature decreases when a better performance material is chosen. For the M470-50A material, the average temperature reduction was 13% and for the M250-35A the average temperature drop was 24%.
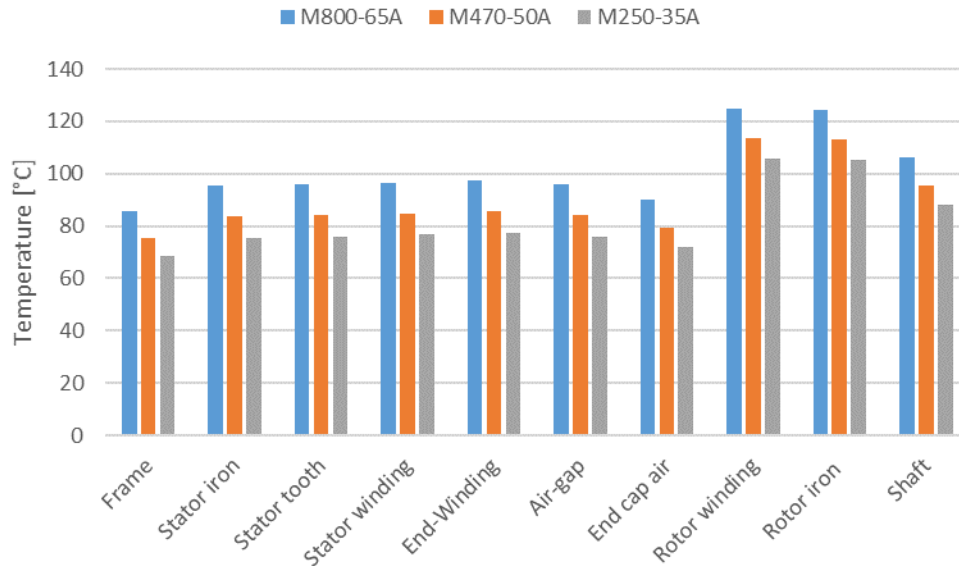
Figure 4.4 Temperature variation with different electrical steel selection *(own source)*.

4.2 Finite element analysis results

In this section, the finite element method technique is implemented to obtain the temperature distribution inside the studied induction machine. In order to do this, a computer aided engineering (CAE) software is used to apply the method and solve the large number of equations.

The first step in the modeling process is to build the motor geometry with the aid of a CAD software and export it in a file type supported by the CAE environment. Figure 4.5 shows the geometry used to solve the heat transfer problem inside the machine. In this model, a steel housing of the machine with its fins are included. The geometry was based in the dimension showed in figure B.1 in annex B.

Because of symmetry properties, only a quarter of the motor needs to be modeled, reducing the number of element and nodes in the domain and thus reducing the computing time. The volume around the machine is set to be air at the ambient temperature and the housing is cooled by the means of natural convection.
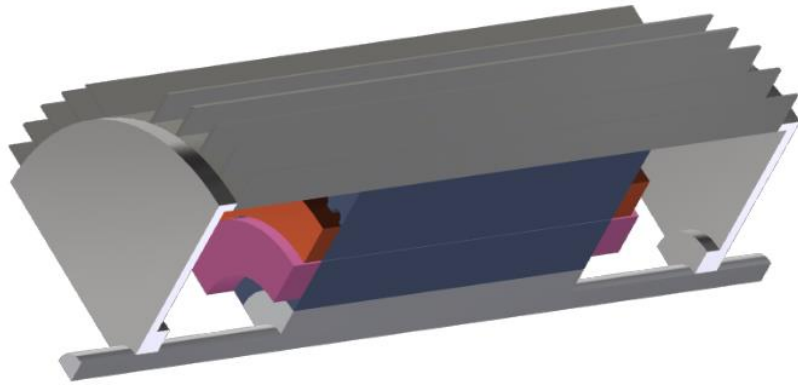
Figure 4.5 Geometry used in the FEA model *(own source).*

The FEA method is based on the subdivision of the domain (in this case the induction machine) in many small elements and to solve that many numbers of equations to find a solution. For this simulation, the machine is stationary, and the movement of the rotor is represented by a convection coefficient in the airgap. Also, the motor is modeled in a steady state thermal environment, so the temperatures found are the ones when heat equilibrium is reach. In this sense, a large number of elements translate in more computation time, so the simplification of the geometry becomes a necessity to limit the number of subdivisions without losing accuracy. Figure 4.6 show some examples of simplifications to the model to improve the performance of the simulations.
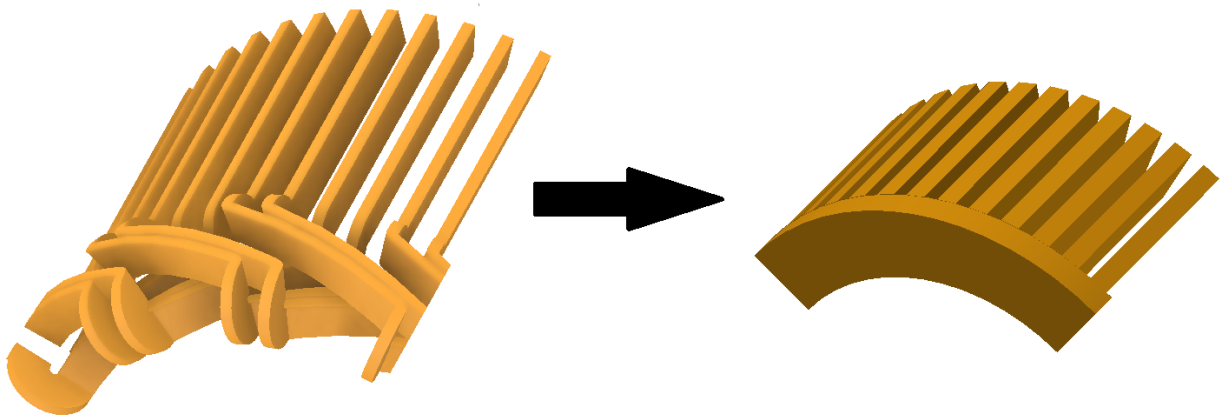
Figure 4.6 Geometry simplification for the windings *(own source)*.

In figure 4.6, the main simplification is the end-winding shape. The left geometry is the closest representation of the real winding, but due to sharp turns in the end-winding portion the meshing of the body was not efficient and translate in bad quality elements and longer simulation times. A torus shape was used to replace this portion, facilitating the subdivision of the volume and improving the performance of the FEA software.

Another case is when the rotor bars present a skew angle of 8.5°. The simplification consists in considering that there is no skew angle. This change allows the simplification of the mesh in the end-ring connections and it and facilitates the symmetry boundary condition in the motor.

The same heat transfer coefficients calculated for the thermal network are used for the FEA simulations and the losses are transformed in a loss density value and is considered that are distributed uniformly along each part. The heat transfer from the housing to the ambient is mainly to natural convection and a low coefficient values is used to simulate this scenario.

Finally, the temperature distribution is presented in figure 4.7.
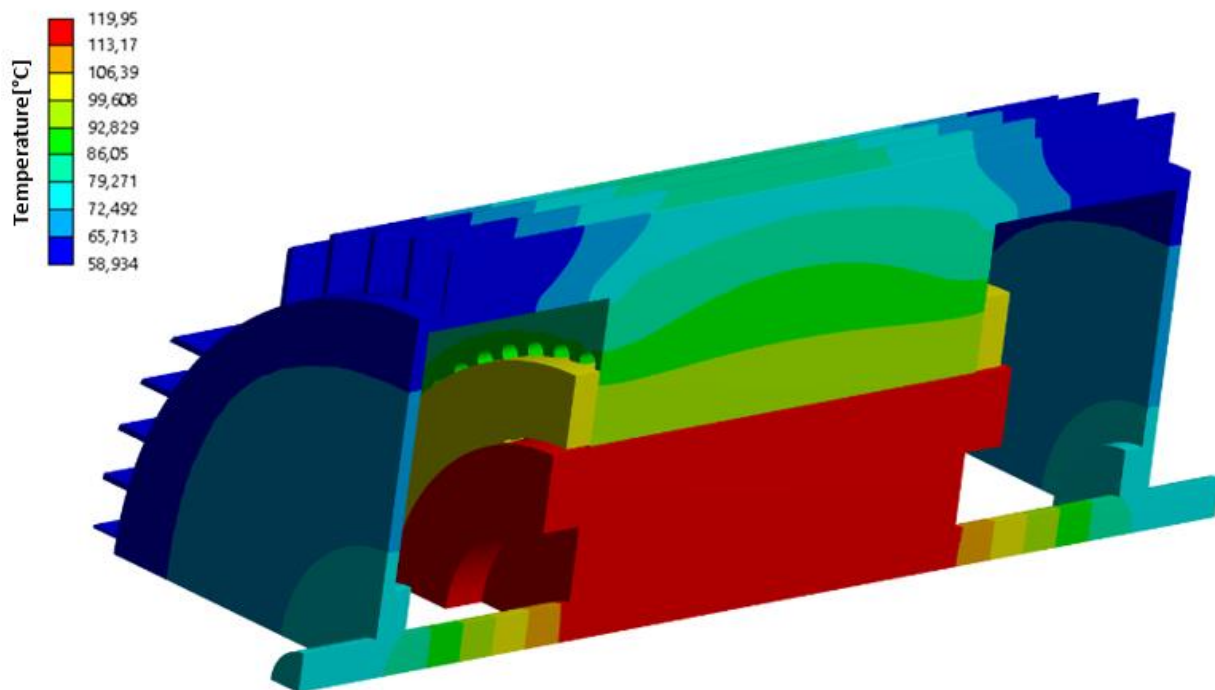
Figure 4.7 Temperature distribution inside the induction motor (FEA results) *(own source).*

From figure 4.7, the higher temperatures are concentrated on the rotor portion of the motor, reaching 120°C for the end-ring part. This is expected due to the lack of ventilation in the motor and the less

contact surface of the shaft with the ambient (which is the main way to evacuate the heat) compared to the housing. Table 4.2 summarize the temperature in the main parts of the induction machine.

Table 4.2 Average temperature of different parts in the motor

Part	Average Temperature [°C]
Frame	87.1
Stator iron	99.3
Stator end-Winding	103.3
Rotor winding	119.9

A sensitivity analysis is also carried out in the FEA case. In table 4.3 the result for the temperature with different electrical steel are summarized.

Table 4.3 Sensitivity analysis comparison

Part	M800-65A		M470-50A		M250-35A	
	LPM	FEA	LPM	FEA	LPM	FEA
Frame	85.86 °C	88.5 °C	75.17 °C	76.92 °C	68.44 °C	69.37 °C
Stator iron	95.42 °C	96.6 °C	83.66 °C	82.54 °C	75.47 °C	75.16 °C
Stator end-winding	101.30 °C	103.2 °C	85.55 °C	86.54 °C	77.37 °C	81.54 °C
Rotor winding	124.69 °C	120.3 °C	113.44 °C	115.32 °C	105.61 °C	112.63 °C

In the context of the software usage to simulate the heat transfer phenomena, Finite volumes method (most used method in CFD) and a FEA software are two option available for the user. In chapter 2, some of the features of these method were commended and in table 4.4 some of the advantages and disadvantages are presented for each technique [62], [63].

Table 4.4 Advantages and disadvantages of each method

Method	Advantages	Disadvantages
Finite element	- Very general method - Easier to increase elements order	Equations and mathematics involved are more complex

	• Easier to handle Multiphysics analysis	• Less physical significance of the method
Finite volumes (CFD)	• Natural choice for fluid problems	• Harder to work with complex geometries

The advantage of the finite element method is the capacity to adapt into any geometry. Hence, this method has a great flexibility in terms of the number of applications that is capable to handle. At the same time, due to the formulation of the method, is easier to increase the polynomial order up to two or three times in the solution process, enhancing the accuracy of the results. Finally, the mathematical foundation of the method makes it easier to couple the different phenomena (for example, electromagnetic and thermal analysis). There also some disadvantages in the method, such as the complexity of the mathematic involve in the formulation, hindering the application for some situation where great expertise is needed. Other problem may be the lack of significance in the mathematics which are not linked with specific physical phenomena, restricting the intuitiveness of the method.

4.3 Validation of the results

In this section, the LPM and FEA results previously obtained are going to be compared with experimental data obtained from measurements done in Lappeenranta University of Technology, Finland by the electric machine team. Figure B.2 in annex B, summarize all the measures, where there are several sensors located mainly in the end-winding area. Table 4.5 shows the comparison between the sensor data and the values obtain from the LPM and FEA.

Table 4.5 Result comparison with the experimental data

Part	Experimental data Temperature (Figure B.2)	LPM Result	LPM error	FEA Result	FEA error
End-winding	104.1 °C	101.3 °C	3.0%	105.1 °C	1.1%
Stator iron	101.9 °C	96.6 °C	5.2%	99.3 °C	2.6%
Rotor iron	119.2 °C	124.5 °C	4.4%	120.9 °C	1.4%
Rotor Winding	118.6 °C	124.7 °C	5.1%	120.8 °C	1.8%

4.4 Conclusion

In this chapter, the temperature distribution for the induction motor was calculated. The lumped parameter method and finite element analysis was used for this purpose.

After the thermal network was built and the temperature for rated values was found, a sensitivity analysis was carried out where some of the parameters of the model were changed to see the results variation in each case. From this, one conclusion is the importance of the material selection in the temperatures obtained. Choosing a lower loss electrical steel or a different shaft material could be determinant in the performance of a motor.

In the FEA study, more precise result was obtained than in the LPM case, but more time developing the model and more computation power were needed. From the comparison between the FEA and FVM methods, the finite element analysis is enough to accomplish good results with respect to the validation vales mainly due to the fact that the induction machine does not have a cooling method, so the main way to evacuate the heat from the motor is through conduction, this is corroborated with the sensitivity analysis results.

Chapter 5. General conclusions and future work

5.1 General conclusions

Two models to obtain the temperature distribution inside an induction machine were built during the realization of this thesis. First, from the electromagnetic analysis and sensitivity analysis in the thermal calculations, one of the main conclusions is the importance of material selection in the design process. Depending on the budget of the project the material choice can play an important role in certain situations.

From the validation results, some of the most important conclusions are shown below:

➢ The two models give temperatures within a 5% of error approximately, which are satisfactory results considering the simplification and considerations made for each one of the methods.

➢ The thermal network built from the lumped parameter model seems to be the best option for this particular motor. The circuit gives good results in this case with a small set-up and computation time required for the solution. But as a disadvantage, the LPM model requires a large amount of time to develop for a different topology. For example, if an axial flux machine thermal network is needed, a brad literature review and experimental testing is required to validate this model.

➢ The Finite element method model takes a larger amount of time to set-up and execute than the LPM counterpart. The advantage is that the same procedure is needed for any geometry, so this model is more flexible and versatile. Another advantage is that the electromagnetic and structural analysis is usually done using FEA, so there is a natural integration if the thermal analysis uses the same technique and the learning time require to properly use CAE software is reduced. As a disadvantage, in a case that the method needs to be applied in a numerical or an open source software, due to the complexity of the mathematics involved may not be the best option.

Using CFD has the advantage of being the most precise method for thermal analysis, since is based on the fluid flow phenomena, so for application where more sophisticated cooling systems are present, such as liquid cooling circuits, water jackets, among others, is the best choice since the convection

coefficients needed for the FEA can be too complex to obtain and the thermal resistances in the interface, solid-fluid are not easier to calculate.

As a final conclusion, this thesis delivers an alternative design workflow, where CFD (the standard in electric machines thermal analysis) is not mandatory and other methods such as LPM thermal network and FEA can be use instead, managing accurate results with the potential of saving time. These results can be used by engineers without much experience in CAE motor design to optimize the process.

5.2 Future work

From this work, a structural analysis can be done to complete the design process. This study can use a FEA approach to ensure a good coupling with the electromagnetic and thermal analysis. Also, could be interesting to have an analytical model, similar to the LPM one and compare the results.

References

[1] M. L. Hosain and R. B. Fdhila, "Air-Gap Heat Transfer in Rotating Electrical Machines: A Parametric Study," *Energy Procedia*, vol. 142, pp. 4176–4181, 2017, doi: 10.1016/j.egypro.2017.12.343.

[2] A. J. Bazurto, E. C. Quispe, and R. C. Mendoza, "Causes and failures classification of industrial electric motor," *Proc. 2016 IEEE ANDESCON, ANDESCON 2016*, no. November 2017, 2017, doi: 10.1109/ANDESCON.2016.7836190.

[3] U. Nations and I. Development, "Energy efficiency in electric motor systems: Technology, saving potentials and policy options developing countries," *Energy Effic. Electr. Mot. Syst. Tech. potentials policy approaches Dev. Ctries.*, no. January, p. 34, 2012.

[4] J. C. Andreas, *Energy-efficient electric motors : selection and application*. M. Dekker, 1992.

[5] B. D. Cullity and C. D. Graham, *Introduction to Magnetic Materials*. Hoboken, NJ, USA: John Wiley & Sons, Inc., 2008.

[6] K. H. J. Buschow and F. R. de Boer, *Physics of Magnetism and Magnetic Materials*. Springer US, 2003.

[7] J. F. Gieras, *Permanent magnet motor technology : design and applications*. CRC Press, 2010.

[8] J. Ciro *et al.*, "New approach to evaluate a non-grain oriented electrical steel electromagnetic performance using photomicrographic analysis via digital image processing," vol. 8, no. 1, pp. 112–126, 2017, doi: 10.1016/j.jmrt.2017.09.007.

[9] M. Anto and C. Paolinelli, "Low core loss non-oriented silicon steels," vol. 320, pp. 2485–2489, 2008, doi: 10.1016/j.jmmm.2008.04.054.

[10] G. Ouyang, X. Chen, Y. Liang, C. Macziewski, and J. Cui, "Journal of Magnetism and Magnetic Materials Review of Fe-6 . 5 wt % Si high silicon steel — A promising soft magnetic material for sub-kHz application," *J. Magn. Magn. Mater.*, vol. 481, no. January, pp. 234–250, 2019, doi: 10.1016/j.jmmm.2019.02.089.

[11] M. Ohta and R. Hasegawa, "Soft magnetic properties of magnetic cores assembled with a high B s Fe – based nanocrystalline alloy," no. October, 2016, doi: 10.1109/TMAG.2016.2620118.

[12] K. Yoon and B. Kwon, "Optimal Design of a New Interior Permanent Magnet Motor Using a Flared-Shape Arrangement of Ferrite Magnets," vol. 52, no. 7, pp. 18–21, 2016.

[13] Z. Li, J. Chen, C. Zhang, L. Liu, and X. Wang, "Cogging Torque Reduction in External-rotor Permanent Magnet Torque Motor Based on Different Shape of Magnet," no. 1, pp. 304–309, 2017.

[14] K. C. Agrawal, *Industrial power engineering and applications handbook*. Newnes, 2001.

[15] "IEC 60085 INTERNATIONAL STANDARD NORME INTERNATIONALE Electrical insulation-Thermal evaluation and designation Isolation électrique-Evaluation et désignation

thermiques," 2007.

[16] Z. Wang and W. Wu, "Effect of higher insulation material thermal conductivity on transformer temperature rise," *34th Electr. Insul. Conf. EIC 2016*, no. June, pp. 358–361, 2016, doi: 10.1109/EIC.2016.7548613.

[17] M. Brockschmidt, F. Pohlmann, S. Kempen, and P. Gröppel, "Testing of Nano-Insulation Materials," no. June, pp. 506–510, 2011.

[18] A. Komodromos, C. Lobbe, and A. E. Tekkaya, "Development of forming and product properties of copper wire in a linear coil winding process," *2017 7th Int. Electr. Drives Prod. Conf. EDPC 2017 - Proc.*, vol. 2017-Decem, pp. 1–7, 2018, doi: 10.1109/EDPC.2017.8328143.

[19] M. Polikarpova *et al.*, "Hybrid Cooling Method of Axial-Flux Permanent-Magnet Machines for Vehicle Applications," *IEEE Trans. Ind. Electron.*, vol. 62, no. 12, pp. 7382–7390, 2015, doi: 10.1109/TIE.2015.2465354.

[20] P. Lindh, I. Petrov, J. Pyrhönen, M. Niemelä, P. Immonen, and E. Scherman, "Direct Liquid Cooling Method verified with a Permanent-Magnet Traction Motor in a Bus," *2018 XIII Int. Conf. Electr. Mach.*, pp. 2472–2477, 2018, doi: 10.1109/ICELMACH.2018.8506807.

[21] C. Rhebergen, B. Bilgin, A. Emadi, E. Rowan, and J. Lo, "Enhancement of electric motor thermal management through axial cooling methods: A materials approach," *2015 IEEE Energy Convers. Congr. Expo. ECCE 2015*, pp. 5682–5688, 2015, doi: 10.1109/ECCE.2015.7310458.

[22] Y. G. Guo, J. G. Zhu, and W. Wu, "Thermal analysis of soft magnetic composite motors using a hybrid model with distributed heat sources," *IEEE Trans. Magn.*, vol. 41, no. 6, pp. 2124–2128, 2005, doi: 10.1109/TMAG.2005.848316.

[23] W. Jara, P. Lindh, J. Tapia, and J. Pyrhonen, "A novel rotor structure for an Axial Flux PM machine: Performance analysis," *2016 Int. Symp. Power Electron. Electr. Drives, Autom. Motion, SPEEDAM 2016*, pp. 237–241, 2016, doi: 10.1109/SPEEDAM.2016.7525871.

[24] M. Jiménez, "Análisis de una máquina eléctrica de flujo axial con bobinados de paso fraccionario e imanes permanentes," Universidad de Concepción, 2019.

[25] Stephen J. Chapman, *Electric Machinery Fundermentals*. 2012.

[26] J. Song-Manguelle, G. Ekemb, D. L. Mon-Nzongo, T. Jin, and M. L. Doumbia, "A theoretical analysis of pulsating torque components in AC machines with variable frequency drives and dynamic mechanical loads," *IEEE Trans. Ind. Electron.*, vol. 65, no. 12, pp. 9311–9324, Dec. 2018, doi: 10.1109/TIE.2018.2823681.

[27] J. Song-Manguelle, G. Ekemb, S. Schroder, T. Geyer, J. M. Nyobe-Yome, and R. Wamkeue, "Analytical expression of pulsating torque harmonics due to PWM drives," in *2013 IEEE Energy Conversion Congress and Exposition, ECCE 2013*, 2013, pp. 2813–2820, doi: 10.1109/ECCE.2013.6647066.

[28] Y. Li, S. Li, and B. Sarlioglu, "Analysis of pulsating torque in squirrel cage induction machines by investigating stator slot and rotor bar dimensions for traction applications," in *2013 IEEE Energy Conversion Congress and Exposition, ECCE 2013*, 2013, pp. 246–253, doi: 10.1109/ECCE.2013.6646707.

[29] F. Parasiliti, R. Petrella, and M. Tursini, "Torque ripple compensation in permanent magnet synchronous motors based on Kalman filter," in *IEEE International Symposium on Industrial Electronics*, 1999, vol. 3, pp. 1333–1338, doi: 10.1109/isie.1999.796897.

[30] D. C. S. R. B. Adhavan, M. S. Birundha, "Torque Ripple Reduction in Permanent Magnet Synchronous Motor using Fuzzy Logic Control," *Aust. J. Basic Appl. Sci.*, vol. 7, no. 7, pp. 61–68, 2013.

[31] D. Guo, F. Chu, and D. Chen, "The unbalanced magnetic pull and its effects on vibration in a three-phase generator with eccentric rotor," *J. Sound Vib.*, vol. 254, no. 2, pp. 297–312, Jul. 2003, doi: 10.1006/jsvi.2001.4088.

[32] A. A. Salah, D. G. Dorrell, and Y. Guo, "A review of the monitoring and damping unbalanced magnetic pull in induction machines due to rotor eccentricity," *IEEE Trans. Ind. Appl.*, vol. 55, no. 3, pp. 2569–2580, 2019, doi: 10.1109/TIA.2019.2892359.

[33] D. G. Dorrell, "Calculation of Unbalanced Magnetic Pull in Cage Induction Machines," University of Cambridge, 1993.

[34] ABB Switzerland Ltd., "Gearless Mill Drives.," *Local Business Unit Process Industries*. 2018.

[35] F. Fiorillo and A. Novikov, "An improved approach to power losses in magnetic laminations under nonsinusoidal induction waveform," *IEEE Trans. Magn.*, vol. 26, no. 5, pp. 2904–2910, 1990, doi: 10.1109/20.104905.

[36] "SKF."   https://www.skf.com/group/products/rolling-bearings/principles-of-rolling-bearing-selection/bearing-selection-process/operating-temperature-and-speed/bearing-friction-power-loss-and-starting-torque (accessed Jul. 11, 2020).

[37] W. Schuisky, *Design of Electrical Machines (Berechnung elektrischer Maschinen).* Springer Verlag, Vienna, 1960.

[38] N. Westerhof, N. Stergiopulos, M. I. M. Noble, and B. E. Westerhof, "Turbulence," in *Snapshots of Hemodynamics*, Cham: Springer International Publishing, 2019, pp. 23–25.

[39] K. M. Becker and J. Kaye, "The Influence of a Radial Temperature Gradient on the Instability of Fluid Flow in an Annulus With an Inner Rotating Cylinder," *J. Heat Transfer*, vol. 84, no. 2, pp. 106–110, May 1962, doi: 10.1115/1.3684306.

[40] A. Choudhary, D. Goyal, S. L. Shimi, and A. Akula, "Condition Monitoring and Fault Diagnosis of Induction Motors: A Review," *Arch. Comput. Methods Eng.*, vol. 26, no. 4, pp. 1221–1238, 2019, doi: 10.1007/s11831-018-9286-z.

[41] J. Pyrhonen, T. Jokinen, and V. Hrabovcova, *Design of Rotating Electrical Machines, 2nd Edition -*. 2013.

[42] T. A. Lipo, *Introduction to AC Machine Design*. Hoboken, NJ, USA: John Wiley & Sons, Inc., 2017.

[43] D. Roberts, "The application of an induction motor thermal model to motor protection and other functions.," University of Liverpool, 1986.

[44] L. Popova, J. Nerg, and J. Pyrhönen, "Combined Electromagnetic and thermal design platform for totally enclosed induction machines," in *SDEMPED 2011 - 8th IEEE Symposium on*

Diagnostics for Electrical Machines, Power Electronics and Drives, 2011, pp. 153–158, doi: 10.1109/DEMPED.2011.6063617.

[45]   M. F. S. Touhami, Y. Bertin, Y. Lefèvre, J. F. Llibre, C. Henaux, "Lumped Parameter Thermal Model of Permanent Magnet Synchronous Machines," vol. 508, no. July, pp. 621–628, 2017, doi: 10.4028/www.scientific.net/MSF.508.621.

[46]   A. M. El-Refaie, N. C. Harris, T. M. Jahns, and K. M. Rahman, "Thermal analysis of multibarrier interior PM synchronous machine using lumped parameter model," *IEEE Trans. Energy Convers.*, vol. 19, no. 2, pp. 303–309, 2004, doi: 10.1109/TEC.2004.827011.

[47]   I. J. Perez and J. G. Kassakian, "A stationary thermal model for smooth air-gap rotating electric machines," *Electr. Mach. Power Syst.*, vol. 3, no. 3–4, pp. 285–303, 1979, doi: 10.1080/03616967908955346.

[48]   O. Mirzapour, S. Karimi-Arpanahi, and H. Oraee, "Evaluating Grid Harmonics Effect on Induction Motor Using Reduced Thermal Model," *Proc. - 2018 Smart Grid Conf. SGC 2018*, 2018, doi: 10.1109/SGC.2018.8777879.

[49]   E. Ghosh, F. Ahmed, A. Mollaeian, J. Tjong, and N. C. Kar, "Online parameter estimation and loss calculation using duplex neural - Lumped parameter thermal network for faulty induction motor," *IEEE CEFC 2016 - 17th Bienn. Conf. Electromagn. F. Comput.*, vol. 55, no. 12, p. 5090, 2017, doi: 10.1109/CEFC.2016.7816406.

[50]   P. S. Ghahfarokhi, A. Kallaste, T. Vaimann, A. Rassolkin, and A. Belahcen, "Steady-state thermal model of a synchronous reluctance motor," in *2018 IEEE 59th Annual International Scientific Conference on Power and Electrical Engineering of Riga Technical University, RTUCON 2018 - Proceedings*, 2018, doi: 10.1109/RTUCON.2018.8659846.

[51]   W. Wang, Y. Zhou, and Y. Chen, "Investigation of lumped-parameter thermal model and thermal parameters test for IPMSM," *2014 17th Int. Conf. Electr. Mach. Syst. ICEMS 2014*, pp. 3246–3252, 2014, doi: 10.1109/ICEMS.2014.7014052.

[52]   R. Burke, A. Giedymin, Z. Wu, H. Chuan, N. Bourne, and J. G. Hawley, "A Lumped Parameter Thermal Model for Single Sided AFPM Machines with Experimental Validation," *IEEE Trans. Transp. Electrif.*, vol. 6, no. 3, pp. 1065–1083, 2020, doi: 10.1109/TTE.2020.2998110.

[53]   N. Rostami, M. R. Feyzi, J. Pyrhonen, A. Parviainen, and M. Niemela, "Lumped-parameter thermal model for axial flux permanent magnet machines," *IEEE Trans. Magn.*, vol. 49, no. 3, pp. 1178–1184, 2013, doi: 10.1109/TMAG.2012.2210051.

[54]   G. Bramerdorfer, J. Tapia, J. Pyrhönen, and A. Cavagnino, "Modern Electrical Machine Design Optimization: Techniques, Trends, and Best Practices," *IEEE Trans. Ind. Electron.*, vol. 65, no. 10, pp. 7672–7684, 2018, doi: 10.1109/TIE.2018.2801805.

[55]   K. Daukaev, A. Rassolkin, A. Kallaste, T. Vaimann, and A. Belahcen, "A review of electrical machine design processes from the standpoint of software selection," in *58th Annual International Scientific Confereence on Power and Electrical Engineering of Riga Technical University, RTUCON 2017 - Proceedings*, Nov. 2017, vol. 2017-November, pp. 1–6, doi: 10.1109/RTUCON.2017.8124818.

[56]   Association of electrical and mechanical trades, "AEMT Journal," vol. 17, no. 3, 2017.

[57]   S. J. Salon, *Finite Element Analysis of Electrical Machines*. Springer US, 1995.

[58]   P. Lindh, L. Aarniovuori, H. Karkkainen, M. Niemela, and J. Pyrhonen, "IM Loss Evaluation Using FEA and Measurements," *Proc. - 2018 23rd Int. Conf. Electr. Mach. ICEM 2018*, pp. 1220–1226, 2018, doi: 10.1109/ICELMACH.2018.8507154.

[59]   L. Aarniovuori, P. Lindh, H. Karkkainen, M. Niemela, J. Pyrhonen, and W. Cao, "Analytical evaluation of high-efficiency induction motor losses," in *2019 IEEE International Electric Machines and Drives Conference, IEMDC 2019*, May 2019, pp. 1501–1507, doi: 10.1109/IEMDC.2019.8785380.

[60]   S. Williamson and M. C. Begg, "Calculation of the resistance of induction motor end rings," *IEE Proc. B Electr. Power Appl.*, vol. 133, no. 2, pp. 54–60, 1986, doi: 10.1049/ip-b.1986.0010.

[61]   F. Fiorillo and A. Novikov, "An Improved Approach to Power Losses in Magnetic Laminations under Nonsinusoidal Induction Waveform," *IEEE Trans. Magn.*, vol. 26, no. 5, pp. 2904–2910, 1990, doi: 10.1109/20.104905.

[62]   S. Geller, M. Krafczyk, J. Tölke, S. Turek, and J. Hron, "Benchmark computations based on lattice-Boltzmann, finite element and finite volume methods for laminar flows," *Comput. Fluids*, vol. 35, no. 8–9, pp. 888–897, 2006, doi: 10.1016/j.compfluid.2005.08.009.

[63]   J. M. Fiard and R. Herbin, "Comparison between finite volume and finite element methods for an elliptic system arising in electrochemical engineering," *Comput. Methods Appl. Mech. Eng.*, vol. 115, no. 3–4, pp. 315–338, 1994, doi: 10.1016/0045-7825(94)90065-5.

Annex A. Thermal resistances calculation detail

In this section, the thermal network details are presented. Figure A.1 shows the final circuit representing the induction motor and table A.1 shows the description of each thermal resistance. The resistance with the R20//R21 value is the result of connecting resistances R20 and R21 in parallel.
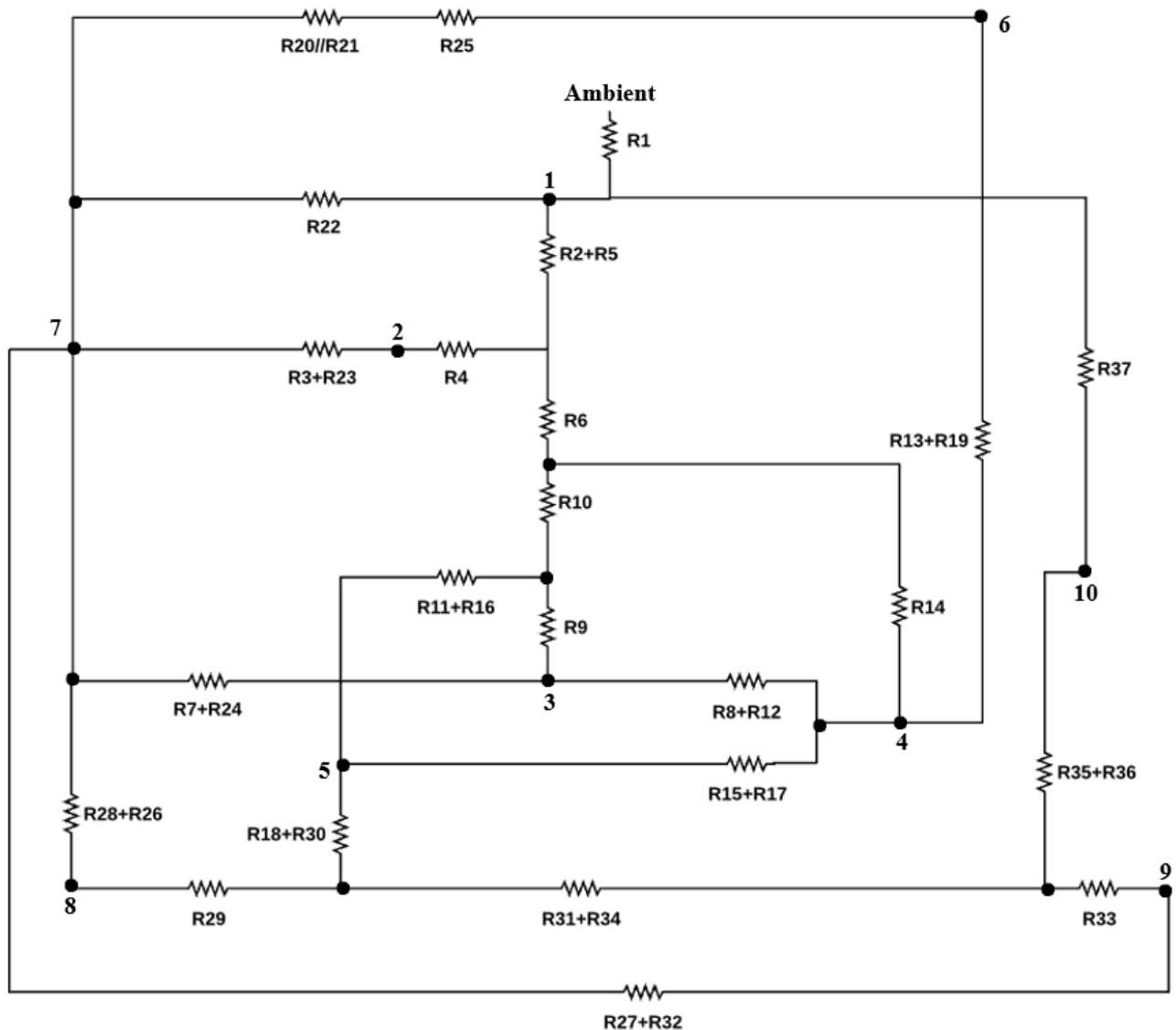

Figure A.1 Induction motor thermal network *(own source).*

Table A.1 Thermal resistances description

Resistance	Description
$R1$	Thermal resistance from frame to ambient
R2	Radial thermal resistance from frame to stator yoke
R3	Axial thermal resistance from stator yoke to end cap air
R4	Radial interconnecting thermal resistance of the stator yoke
R5	Radial thermal resistance from the stator yoke to frame
R6	Radial thermal resistance from the stator yoke to stator teeth
R7	Axial thermal resistance from stator teeth to end cap air
R8	Radial thermal resistance from stator teeth to stator winding
R9	Radial interconnecting thermal resistance of the stator teeth
R10	Radial thermal resistance from the stator teeth to stator yoke
R11	Radial thermal resistance from the stator teeth to air gap
R12	Radial thermal resistance from the stator winding to stator teeth
R13	Axial thermal resistance from the stator slots to end-winding
R14	Radial thermal resistance from the stator coils to stator yoke
R15	Radial thermal resistance from the stator coils to air gap
R16	Radial thermal resistance from the air gap to stator teeth
R17	Radial thermal resistance from the air gap to stator coils
R18	Radial thermal resistance from the air gap to the rotor winding
R19	Axial thermal resistance from the end-winding to stator winding
R20	Thermal resistance from the end-winding to end cap air
R21	Thermal resistance from the end-winding to end cap air
R22	Axial thermal resistance from the end cap air to frame
R23	Axial thermal resistance from the end cap air to stator yoke
R24	Thermal resistance from the end cap air to stator teeth
R25	Thermal resistance from the end cap air to end-winding
R26	Thermal resistance from the end cap air to rotor end-rings
R27	Thermal resistance from the end cap air to rotor iron
R28	Axial thermal resistance from the rotor bars to end cap air
R29	Radial interconnecting thermal resistance of the rotor bars

R30	Radial thermal resistance from the rotor bars to air gap
R31	Radial thermal resistance from the rotor bars to rotor iron
R32	Axial thermal resistance from the rotor iron to end cap air
R33	Radial interconnecting thermal resistance of the rotor iron
R34	Radial thermal resistance from the rotor iron to rotor bars
R35	Radial thermal resistance from the rotor iron to shaft
R36	Radial thermal resistance from the shaft to rotor iron
R37	Axial thermal resistance from the shaft to frame through bearings

A.1 Frame

The frame consists mainly in a hollow cylinder with fins pointing in the radial direction. Figure A.2 shows the frame and the thermal circuit associated with the part.
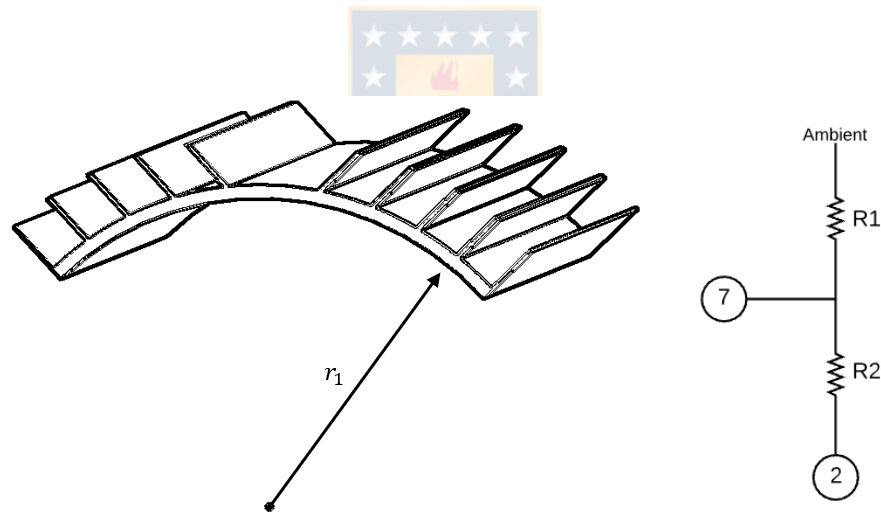
Figure A.2 Frame with the respective thermal network *(own source).*

The resistances in figure A.2 can be calculated as

$$R1 = \frac{1}{\lambda_1 S_{frame}} \tag{A.1}$$

$$R2 = \frac{1}{\pi \lambda_{cont} l r_1} \tag{A.2}$$

where, λ_1 is the heat transfer coefficient between the frame and the ambient obtained using equations (2.22), (2.24) and (2.25) from section 2.3, S_{frame} is the frame surface area where the effect of the fins in the heat transfer process are included in this value, l is the stack length, λ_{cont} is the frame-core contact conductance [43] and r_1 is the stator outer radius.

A.2 Stator iron and stator teeth

The stator yoke can be considered a hollow cylindrical element. The anisotropy effect due to the lamination insulation and the stacking factor are considered. The teeth are modeled as a series of small cylinders thermally connected in parallel. Figure A.3 shows the geometry and the thermal networks.

Figure A.3 Stator iron geometry, Stator yoke (left) and stator teeth (right) thermal networks *(own source).*
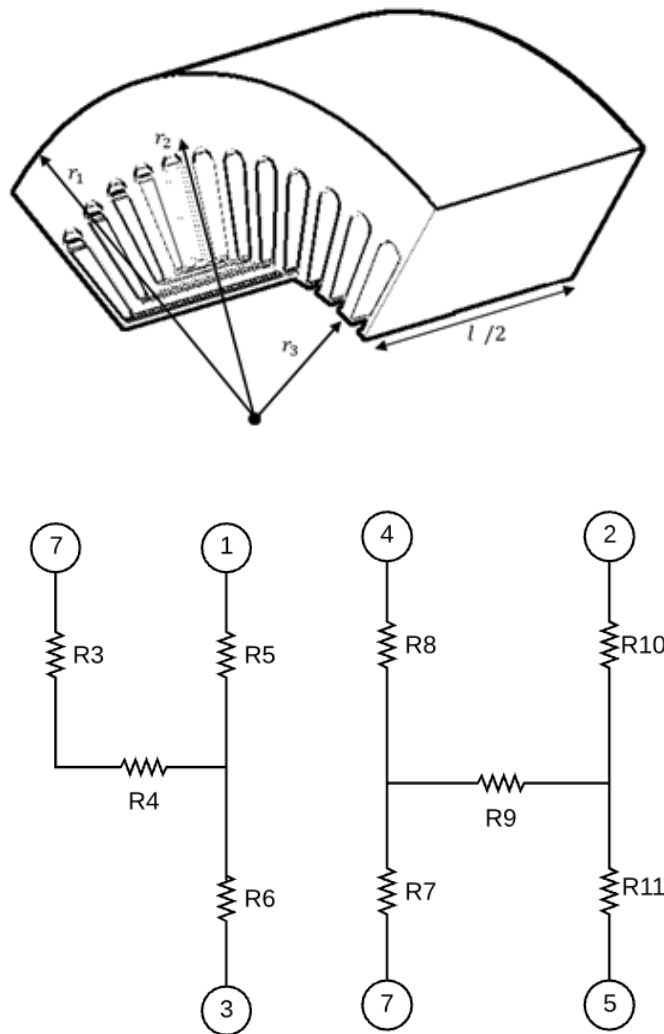
The thermal resistances can be calculated as

$$R3 = \frac{l}{6\pi\lambda_{la}(r_1^2 - r_2^2)} \tag{A.3}$$

$$R4 = \frac{-1}{4\pi\lambda_{lr}ls(r_1^2 - r_2^2)}\left[r_1^2 + r_2^2 - \frac{4r_1^2 r_2^2 \ln\left(\frac{r_1}{r_2}\right)}{r_1^2 - r_2^2}\right] \tag{A.4}$$

$$R5 = \frac{1}{2\pi\lambda_{lr}ls}\left[1 - \frac{2r_2^2 \ln\left(\frac{r_1}{r_2}\right)}{r_1^2 - r_2^2}\right] \tag{A.5}$$

$$R6 = \frac{1}{2\pi\lambda_{lr}ls}\left[\frac{2r_1^2 \ln\left(\frac{r_1}{r_2}\right)}{r_1^2 - r_2^2} - 1\right] \tag{A.6}$$

$$R7 = \frac{l\tau_u}{6\pi\lambda_{la}b_{ds}(r_2^2 - r_3^2)} \tag{A.7}$$

$$R8 = \frac{\pi b_{ds}(r_2^2 - r_3^2)}{\lambda_{lr}ls\tau_u(r_2^2 - r_3^2)^2 n^2} \tag{A.8}$$

$$R9 = \frac{-1}{4\pi\lambda_{lr}lsb_{ds}(r_2^2 - r_3^2)}\left[r_2^2 + r_3^2 - \frac{4r_2^2 r_3^2 \ln\left(\frac{r_2}{r_3}\right)}{r_2^2 - r_3^2}\right] \tag{A.9}$$

$$R10 = \frac{\tau_u}{2\pi\lambda_{lr}lsb_{ds}}\left[1 - \frac{2r_3^2 \ln\left(\frac{r_2}{r_3}\right)}{r_2^2 - r_3^2}\right] \tag{A.10}$$

$$R11 = \frac{\tau_u}{2\pi\lambda_{lr}lsb_{ds}}\left[\frac{2r_2^2 \ln\left(\frac{r_2}{r_3}\right)}{r_2^2 - r_3^2} - 1\right] \tag{A.11}$$

where, λ_{la} and λ_{lr} are the lamination axial and radial thermal conductivity respectively, r_2 is the tooth outer radius, r_3 is the stator inner radius, τ_u is the tooth pitch, b_{ds} is the stator tooth width, n is the number of slots and s is the lamination stacking factor.

A.3 Stator winding and stator end-winding

The windings can be modelled as parallel rods with the same copper and insulation volume as the original part. The end winding is considered a homogenous body with a toroid shape. Figure A.4 present this situation.
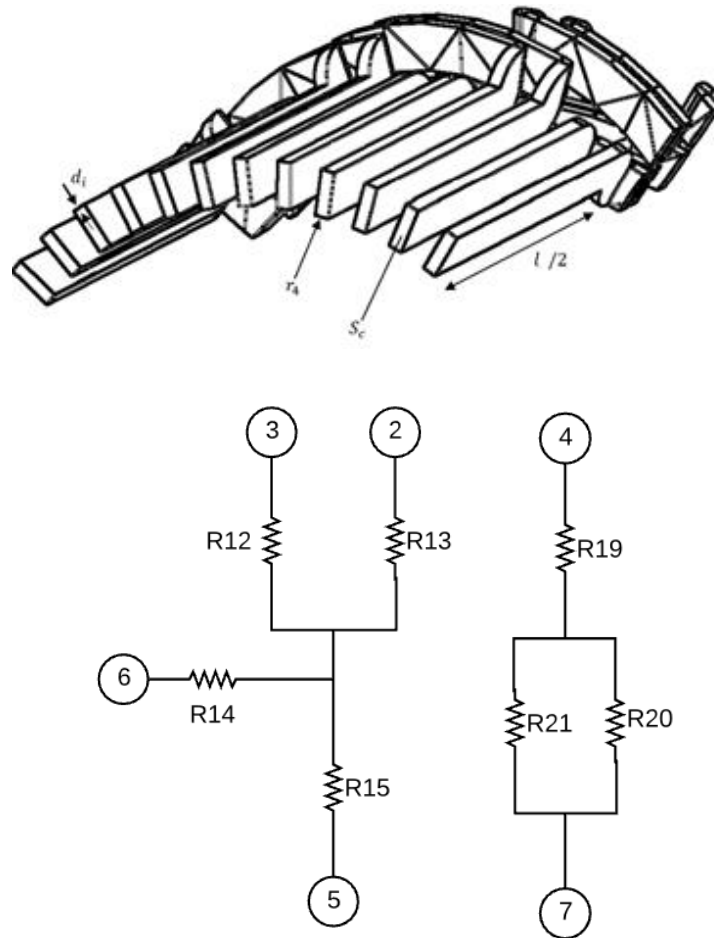
Figure A.4 Geometry, stator winding (left) and stator end-winding (right) thermal network *(own source).*

The thermal resistances are calculated as shown below,

$$R12 = \frac{2d_i}{\pi\lambda_i lr_4 n} + \frac{1}{2\pi\lambda_v lFn} \tag{A.12}$$

$$R13 = \frac{l}{6\lambda_{cu}S_c n} \tag{A.13}$$

$$R14 = \frac{4d_i}{\pi \lambda_i l r_4 n} + \frac{1}{\pi \lambda_v l F n} \tag{A.14}$$

$$R15 = \frac{1}{\pi \lambda_v l F n} \tag{A.15}$$

$$R19 = \frac{l_0 \omega}{n S_c \lambda_{cu}} \tag{A.16}$$

$$R20 = \frac{\omega}{16\pi^2 r_t F \lambda_v} \tag{A.17}$$

$$R21 = \frac{\omega r_6^2}{8\pi r_4^2 l_0 F \lambda_v n} \tag{A.18}$$

where, r_4 is the equivalent winding radius, d_i is the insulation thickness, S_c is the copper cross section area in the slots, F is the radial conductivity factor, λ_{cu} is the copper thermal conductivity, λ_i is the slot liner thermal conductivity, λ_v is the varnish conductivity, r_t is the end-winding toroid radius, r_6 is the end-winding cross-section radius, l_o is the slot winding overhang and ω is the hot-spot to mean temperature ratio.

A.4 Air gap

Since the material of contact with the stator and rotor is air, the convection is taking into account. Figure A.5 shows the thermal network which is the same for the axial and radial resistance.
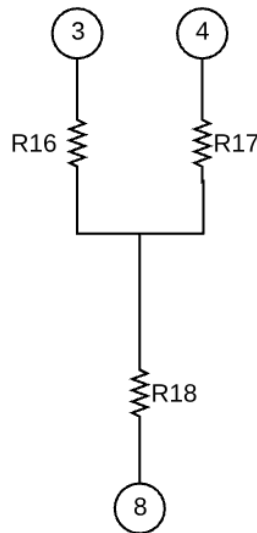
Figure A.5 Airgap thermal network *(own source).*

the thermal resistances are

$$R16 = \frac{\tau_u}{b_{ds}\pi r_3 l\lambda_{2r}\lambda_{2s}} \tag{A.19}$$

$$R17 = \frac{\tau_u}{(\tau_u - b_{ds})\pi r_3 l\lambda_{2r}\lambda_{2s}} \tag{A.20}$$

$$R18 = \frac{1}{\pi r_5 l\lambda_{2r}\lambda_{2s}} \tag{A.21}$$

Here r_5 is the rotor outer radius, λ_{2r} is the rotating air gap film coefficient and λ_{2s} is the stationary air gap film coefficient determined from the equations found in section 2.3 about the convective heat transfer coefficients.

A.5 End cap air

This is the region of air at the front and back of the motor in contact with all the components. The temperature in this volume is assumed to be uniform and only one heat transfer coefficient describes the convection process with all surfaces. Figure A.6 shows the thermal circuit.
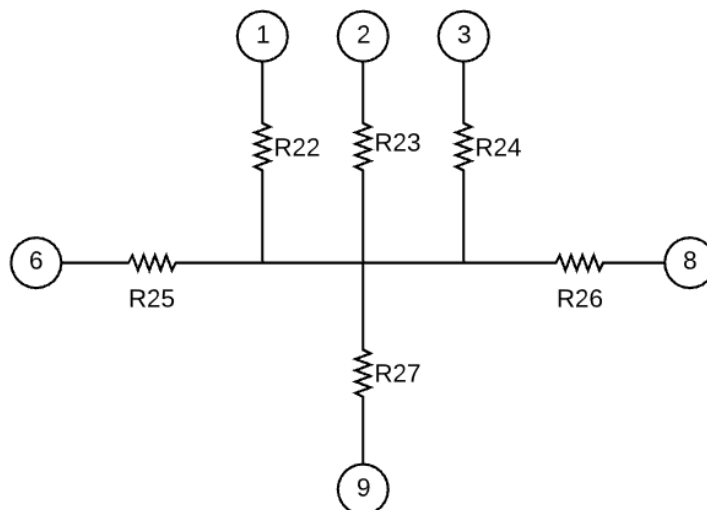
Figure A.6 Thermal network for the end cap air *(own source).*

The thermal resistances can be calculated as,

$$R22 = \frac{1}{S_1 \lambda_{3r} \lambda_{3s}} \tag{A.22}$$

$$R23 = \frac{1}{S_2 \lambda_{3r} \lambda_{3s}} \tag{A.23}$$

$$R24 = \frac{1}{S_3 \lambda_{3r} \lambda_{3s}} \tag{A.24}$$

$$R25 = \frac{1}{1.5 S_4 \lambda_{3r} \lambda_{3s}} \tag{A.25}$$

$$R26 = \frac{1}{S_5 \lambda_{3r} \lambda_{3s}} \tag{A.26}$$

$$R27 = \frac{1}{S_6 \lambda_{3r} \lambda_{3s}} \tag{A.27}$$

Where, S_1 is the contact area of the end cap, S_2 is the contact area of the stator iron, S_3 is contact areas of the stator teeth, S_4 is the contact area of the end-winding portion, S_5 is the contact areas of the rotor end-ring, S_6 is the contact area of the rotor iron, λ_{3r} is the rotating end cap film coefficient and λ_{3s} is the stationary end cap film coefficient.

A.6 Rotor winding

The rotor winding can be modelled as a continuous cylinder with the same volume as the rotor cage. The end ring is effectively a torus. Figure A.7 shows the thermal network.
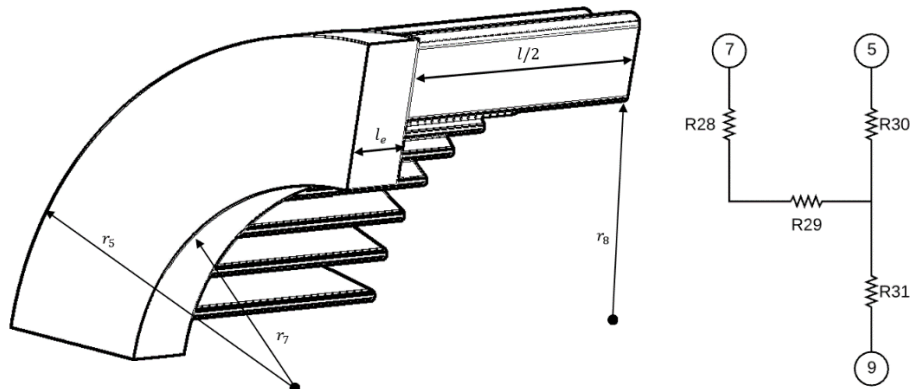
Figure A.7 Rotor winding *(own source).*

The thermal resistances are,

$$R28 = \frac{l}{6\pi\lambda_a(r_5^2 - r_8^2)} + \frac{l_e}{\pi\lambda_a(r_5^2 - r_7^2)} \tag{A.28}$$

$$R29 = \frac{-1}{4\pi\lambda_a l(r_5^2 - r_8^2)} \left[r_5^2 + r_8^2 - \frac{4r_5^2 r_8^2 \ln\left(\frac{r_5}{r_8}\right)}{r_5^2 - r_8^2} \right] \tag{A.29}$$

$$R30 = \frac{1}{2\pi\lambda_a l} \left[1 - \frac{2r_8^2 \ln\left(\frac{r_5}{r_8}\right)}{r_5^2 - r_8^2} \right] \tag{A.30}$$

$$R31 = \frac{1}{2\pi\lambda_a l} \left[\frac{2r_5^2 \ln\left(\frac{r_5}{r_8}\right)}{r_5^2 - r_8^2} - 1 \right] \tag{A.31}$$

Where, r_7 is the end-ring inner radius, r_8 is the equivalent rotor winding radius, l_e is the end-ring width and λ_a is the aluminum thermal conductivity.

A.7 Rotor iron

Here, the same considerations are made as for the stator iron case.
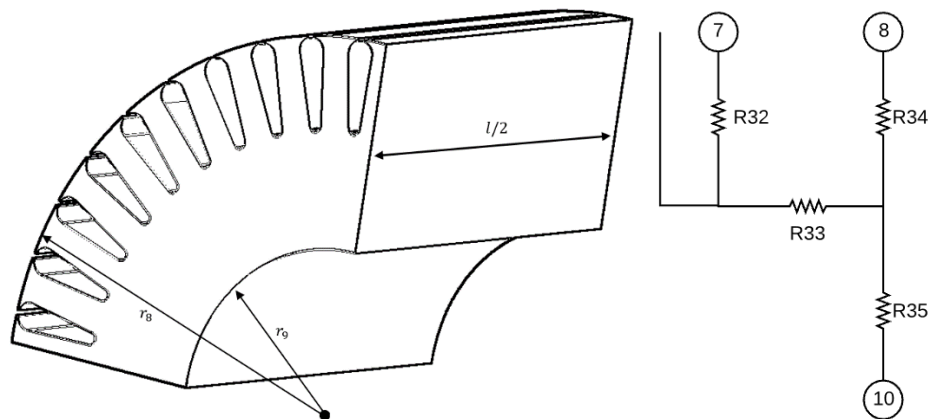
Figure A.8 Rotor iron *(own source).*

The thermal resistances are,

$$R32 = \frac{l}{6\pi\lambda_{la}(r_8^2 - r_9^2)} \tag{A.32}$$

$$R33 = \frac{-1}{4\pi\lambda_{lr}ls(r_8^2 - r_9^2)}\left[r_9^2 + r_8^2 - \frac{4r_9^2 r_8^2 \ln\left(\frac{r_8}{r_9}\right)}{r_8^2 - r_9^2}\right] \tag{A.33}$$

$$R34 = \frac{r_8^2 - r_9^2}{2\pi\lambda_{ls}ls(r_8^2 - r_9^2)}\left[1 - \frac{2r_9^2 \ln\left(\frac{r_8}{r_9}\right)}{r_8^2 - r_9^2}\right] \tag{A.34}$$

$$R35 = \frac{r_8^2 - r_9^2}{2\pi\lambda_{ls}ls(r_8^2 - r_9^2)}\left[\frac{2r_8^2 \ln\left(\frac{r_8}{r_9}\right)}{r_8^2 - r_9^2} - 1\right] \tag{A.35}$$

Where, r_9 is the shaft radius.

A.8 Shaft

The shaft is a simple cylindrical component with no heat generation.
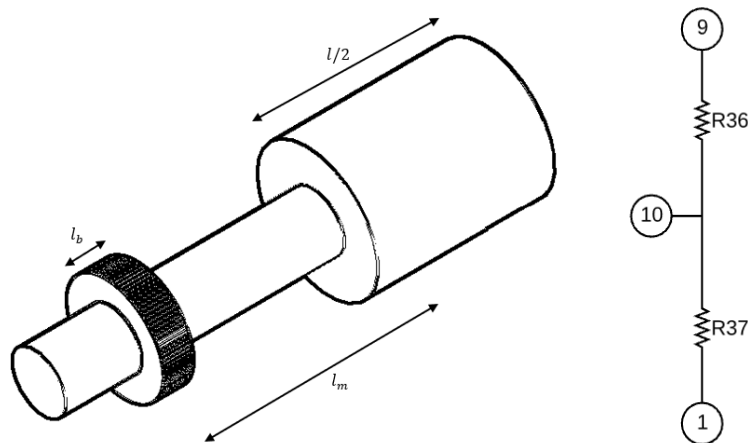
Figure A.9 Shaft *(own source).*

The thermal resistances shown in figure A.8 can be calculated as

$$R36 = \frac{1}{2\pi\lambda_S l} + \frac{l_m}{2\pi\lambda_s r_9^2} \tag{A.36}$$

$$R37 = \frac{1}{4\pi\lambda_S l_b} + \frac{l_m}{2\pi\lambda_s r_9^2} \tag{A.37}$$

Here, l_b is the bearing width, l_m is the distance of the bearing center to the rotor mean and λ_s is the shaft thermal conductivity.

Annex B. Additional figures and tables.
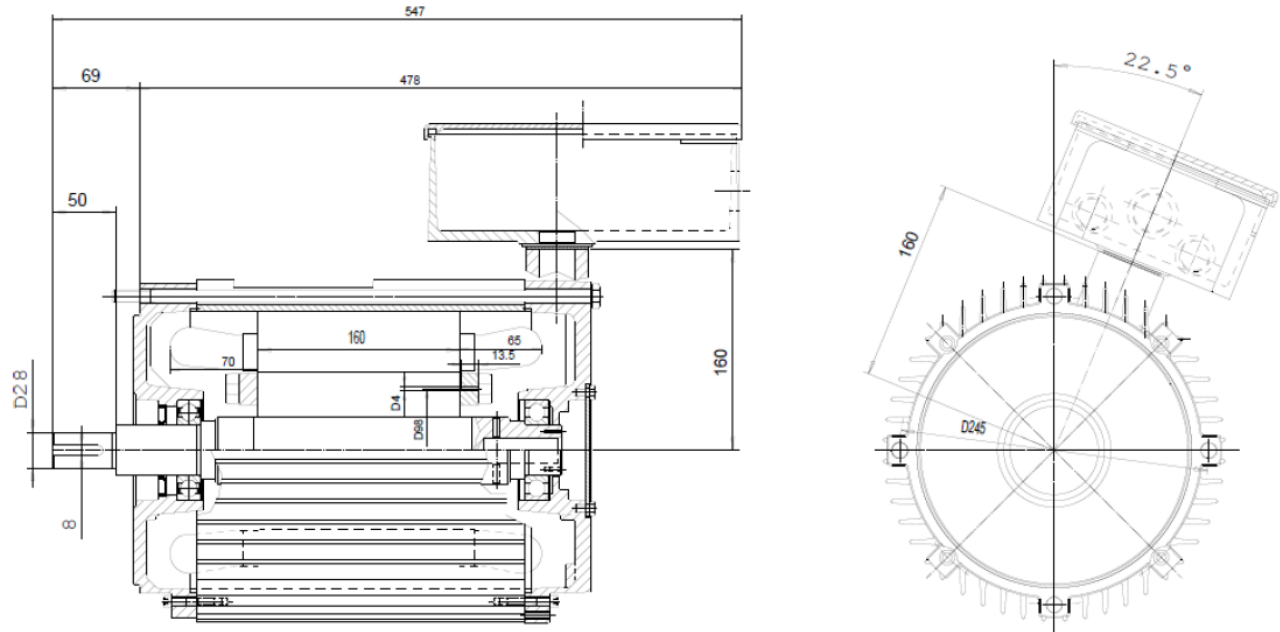
Figure B.1 Induction motor main dimensions.

Table B.1 B-H curve data.

Magnetic flux density [T]	Magnetic flux intensity [A/m]
0	0
0.1	74.7
0.2	97.5
0.3	110
0.4	120
0.5	130
0.6	140
0.7	150
0.8	162
0.9	175
1.0	190
1.1	208
1.2	227
1.3	265
1.4	366
1.5	633
1.6	1490
1.7	3670
1.8	7420

Table B.2 Power-loss curve data.

Magnetic flux density [T]	Loss density [W/kg]
0	0
0.1	0.05
0.2	0.19
0.3	0.41
0.4	0.67
0.5	0.96
0.6	1.29
0.7	1.66
0.8	2.06
0.9	2.52
1.0	3.02
1.1	3.59
1.2	4.22
1.3	4.96
1.4	5.81
1.5	6.74
1.6	7.72
1.7	8.58
1.8	9.25

Table B.3 LPM temperature results.

Part	Temperature [°C]
Frame	85,8574
Stator iron	95,4163
Stator tooth	95,84
Stator winding	96,6378
End-Winding	97,3042
Airgap	95,8878
Endcap air	90,0124
Rotor winding	124,6963
Rotor iron	124,489
Shaft	106,021

Temperature readings

At 50 Hz and rated load

D-end

Sensor	Temp. (°C)	Location
7	98.0	End winding
8	94.7	End winding
9	96.9	End winding
13	99.2	Stator iron
14	96.9	Stator iron
15	98.1	Stator iron

In the middle

Sensor	Temp. (°C)	Location
1	103.6	Stator slot
2	102.6	Stator slot
3	103.8	Stator slot
16	95.9	In the middle of stator iron

N-end

Sensor	Temp. (°C)	Location
4	104.8	End winding
5	106.2	End winding
6	105.9	End winding
10	106.4	Stator iron
11	106.3	Stator iron
12	104.8	Stator iron
17	118.6	Rotor end ring
18	119.2	Rotor yoke

Pt100-sensors

N-end

D-end

N-end

D-end

Rotor: 17 in the end-ring and 18 in the yoke
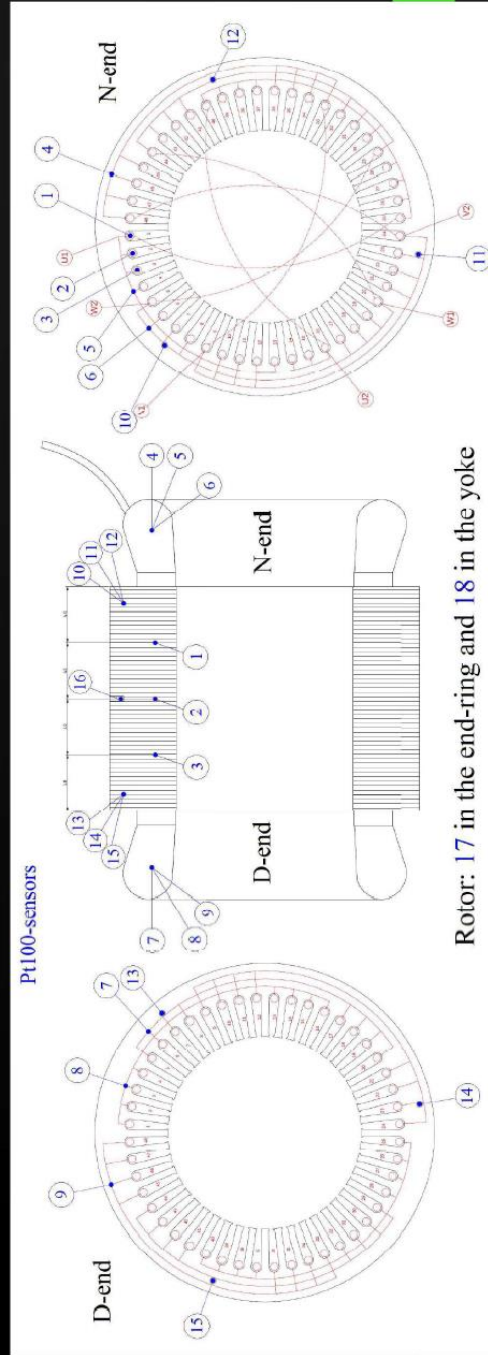
Figure B.2 Sensor data for thermal test.

Annex C.   MATLAB script details.

```
%% INDUCTION MOTOR PARAMENTERS

lp=0.16;                                      % Stack length
r1=0.110;                                     % STATOR OUTER RADIUS
r2=0.0911;                                    % TOOTH OUTER RADIUS
tau_u=0.012;                                  % TOOTH PITCH
n=48;                                         % STATOR SLOTS
S_slot=1.5178e-4;                             % AREA OF SLOT
k_cu=0.7;                                     % COPPER FILL FACTOR
b_ds=6.8;                                     % slot width
r3=0.0625;                                    % TOOTH INNER RADIUS
r4=sqrt(S_slot/pi);                           % EQUIVALENT WINDING RADIUS
di=0.0004;                                    % INSULATION THICKNESS
Sc=S_slot*k_cu;                               % COPPER CROSS SECTION IN THE
SLOTS
Dr=0.0620;                                    % ROTOR OUTER DIAMETER
r5=Dr/2;                                      % ROTOR OUTER RADIUS
rt=(r2+r3)/2;                                 % END-WINDING TORIOD RADIUS
r6=sqrt(Sc/pi)*3.5;                           % END WINDING CROSS SECTION
RADIUS
L0=0.0135;                                    % SLOT WINDING OVERHANG
r7=0.0360;                                    % END DISK INNER RADIUS
r8=0.0490;                                    % EQUIVALENT ROTOR WINDING
RADIUS
le=0.0150;                                    % END DISK WIDTH
r9=0.0270;                                    % SHAFT RADIUS
lm=0.150;                                     % DISTANCE OF BEARING CENTER TO
ROTOR MEAN
lb=0.012;                                     % BEARING HOUSING WIDTH
r_frame=r1+0.0;                               % FRAME RADIUS
D_frame=r_frame*2;                            % FRAME DIAMETER
l_endcap=lm+lb/2-lp/6;                        % ENDCAP LENGTH
l_frame=(lm+lb/2)+lp/3;                       % FRAME LENGTH


S1=(2*pi*r_frame*l_endcap)+(pi*r_frame^2);    % CONTACT AREA OF ENDCAP
S2=pi*(r1^2-r2^2);                            % CONTACT AREA OF STATOR IRON
S3=pi*(r2^2-r3^2)-S_slot*n;                   % CONTACT AREA OF STATOR TEETH
S4=2*pi*r6*(2*pi*rt);                         % CONTACT AREA OF END WINDING
S5=pi*(r5^2-r7^2);                            % CONTACT AREA OF ROTOR END DISK
S6=pi*(r7^2-r9^2);                            % CONTACT AREA OF ROTOR IRON
S_frame=pi*r_frame^2+2*pi*r_frame*l_frame;    % SURFACE AREA OF FRAME

%%  HEAT TRANSFER COEFFICIENTS AND CONDUCTIVITIES

lambda_cont=400;                              % FRAME-CORE CONTACT COEFFICIENT
[W/m2 K]
s=0.97;                                       % LAMINATION STACKING FACTOR
Fr=2.5;                                       % RADIAL CONDUCTIVITY FACTOR
w=1.5;                                        % HOTSPOT TO MEAN TEMPERATURE
RATIO

lambda_la=4;                                  % LAMINATION AXIAL CONDUCTIVITY
OF IRON
```

```
lambda_lr=45;                              % LAMINATION RADIAL CONDUCTIVITY OF IRON
lambda_s=80;                               % SHAFT CONDUCTIVITY
lambda_c=400;                              % COPPER CONDUCTIVITY
lambda_i=0.8;                              % SLOT LINER CONDUCTIVITY
lambda_v=0.8;                              % VARNISH CONDUCTIVITY
lambda_a=237;                              % ALUMINIUM CONDUCTIVITY
lambda_air=0.026;                          % AIR THERMAL CONDUCTIVITY


%% RESISTANCES CALCULATION

R1=1/(2*lambda_1*1.3*S_frame);
R2=1/(pi*lambda_cont*lp*r1);
R3=lp/(6*pi*lambda_la*(r1^2-r2^2));
R4=(-1*(r1^2+r2^2-((4*r1^2*r2^2*log(r1/r2))/(r1^2-
r2^2)))))/(4*pi*lambda_lr*lp*s*(r1^2-r2^2));
R5=(1-((2*r2^2*log(r1/r2))/(r1^2-r2^2)))/(2*pi*lambda_lr*lp*s);
R6=(((2*r1^2*log(r1/r2))/(r1^2-r2^2))-1)/(2*pi*lambda_lr*lp*s);
R7=(lp*tau_u)/(6*pi*lambda_lr*b_ds*(r2^2-r3^2));
R8=(pi*b_ds*(r2^2-r3^2))/(lambda_lr*lp*s*tau_u*(r2-r3)^2*n^2);
R9=(-tau_u*(r2^2+r3^2-((4*r2^2*r3^2*log(r2/r3))/(r2^2-
r3^2))))/(4*pi*lambda_lr*lp*s*b_ds*(r2^2-r3^2));
R10=(tau_u*(1-((2*r3^2*log(r2/r3))/(r2^2-r3^2))))/(2*pi*lambda_lr*lp*s*b_ds);
R11=(tau_u*(((2*r2^2*log(r2/r3))/(r2^2-r3^2))-1))/(2*pi*lambda_lr*lp*s*b_ds);
R12=(2*di/(pi*lambda_i*lp*r4*n))+(1/(2*pi*lambda_v*lp*Fr*n));
R13=lp/(6*pi*lambda_c*Sc*n);
R14=(4*di/(pi*lambda_i*lp*r4*n))+(1/(pi*lambda_v*lp*Fr*n));
R15=1/(pi*lambda_v*lp*Fr*n);
R16=tau_u/(b_ds*pi*r3*lp*lambda_2r);
R17=tau_u/((tau_u-b_ds)*pi*r3*lp*lambda_2r);
R18=1/(pi*r5*lp*lambda_2r);
R19=L0*w/(n*Sc*lambda_c);
R20=w/(16*pi^2*rt*Fr*lambda_v);
R21=(w*r6^2)/(8*pi*r4^2*L0*Fr*lambda_v*n);
R22=1/(S1*lambda_3r);
R23=1/(S2*lambda_3r);
R24=1/(S3*lambda_3r);
R25=1/(1.5*S4*lambda_3r);
R26=1/(S5*lambda_3r);
R27=1/(S6*lambda_3r);
R28=(lp/(6*pi*lambda_a*(r5^2-r8^2)))+(le/(pi*lambda_a*(r5^2-r7^2)));
R29=(-1/(4*pi*lambda_a*lp*(r5^2-r8^2)))*(r5^2+r8^2-
((4*r5^2*r8^2*log(r5/r8))/(r5^2-r8^2)));
R30=(1/(2*pi*lambda_a*lp))*(1-((2*r8^2*log(r5/r8))/(r5^2-r8^2)));
R31=(1/(2*pi*lambda_a*lp))*(((2*r5^2*log(r5/r8))/(r5^2-r8^2))-1);
R32=lp/(6*pi*lambda_la*(r8^2-r9^2));
R33=(-1/(4*pi*lambda_lr*s*(r8^2-r9^2)))*(r8^2+r9^2-
((4*r8^2*r9^2*log(r8/r9))/(r8^2-r9^2)));
R34=((r8^2-r9^2)/(2*pi*lambda_lr*lp*s*(r8^2-r9^2)))*(1-
((2*r9^2*log(r8/r9))/(r8^2-r9^2)));
R35=((r8^2-r9^2)/(2*pi*lambda_lr*lp*s*(r8^2-r9^2)))*(((2*r8^2*log(r8/r9))/(r8^2-
r9^2))-1);
R36=(1/(2*pi*lambda_s*lp))+(lm/(2*pi*lambda_s*r9^2));
R37=(1/(4*pi*lambda_s*lb))+(lm/(2*pi*lambda_s*r9^2));


%% THERMAL CONDUCTANCES
```

```
g12=1/(R2+R4+R5);
g17=1/R22;
g110=1/R37;
g11=g12+g17+g110+1/R1;
g23=1/(R4+R6+R9+R10);
g24=1/(R14+R6+R4);
g25=1/(R4+R6+R10+R11+R16);
g27=1/(R3+R23);
g22=g12+g23+g24+g27;
g34=1/(R8+R12);
g35=1/(R9+R11+R16);
g37=1/(R7+R24);
g33=g23+g34+g35+g37;
g45=1/(R15+R17);
g46=1/(R13+R19);
g44=g24+g34+g45+g46;
g58=1/(R18+R29+R30);
g55=g35+g45+g58;
g67=1/(R25+((R20*R21)/(R20+R21)));
g66=g46+g67;
g78=1/(R26+R28);
g79=1/(R32+R27);
g77=g17+g27+g37+g67+g78+g79;
g89=1/(R29+R31+R33+R34);
g88=g58+g78+g89;
g910=1/(R33+R35+R36);
g99=g89+g910+g79;
g1010=g910+g110;


G=[g11 -g12 0 0 0 0 -g17 … 0 0 0 -g910 g1010];          % Conductance matrix

P=[0 Pfe_yoke/2 (Pfe_teeth+0.3*P_ad)/2 (P_cu*0.48+P_ad*0.4)/2 0  % Losses Vector
P_cu*0.52/2 0 P_al/2 0.3*P_ad/2 0]';

T_amb=[31.7 31.7 31.7 31.7 31.7 31.7 31.7 31.7 31.7 31.7]';

dT=G\P;

T=T_amb+dT;
```